2015-03-01

Radio Emission Toward Regions of Massive Star Formation in the Large Magellanic Cloud

Adam Johanson
Brigham Young University - Provo

Radio Emission Toward Regions of Massive Star Formation in the Large Magellanic Cloud

Adam K. Johanson

A dissertation submitted to the faculty of
Brigham Young University
in partial fulfillment of the requirements for the degree of

Doctor of Philosophy

Victor Migenes, Chair
Clark G. Christensen
Timothy W. Leishman
J. Ward Moody
Denise Stephens

Department of Physics and Astronomy

Brigham Young University

March 2015

ABSTRACT

Radio Emission Toward Regions of Massive Star Formation
in the Large Magellanic Cloud

Adam K. Johanson
Department of Physics and Astronomy, BYU
Doctor of Philosophy

Four regions of massive star formation in the Large Magellanic Cloud (LMC) were observed for water and methanol maser emission and radio continuum emission. A total of 42 radio detections were made including 27 new radio sources, four water masers, and eight compact H II regions. The lobes of a radio galaxy were resolved for the first time, and the host galaxy identified. Seven sources were associated with known massive young stellar objects (YSOs). A multi-wavelength analysis using both the infrared and radio spectrum was used to characterize the sources. Mid-infrared color-magnitude selection criteria for ultracompact H II (UCHII) regions in the LMC are presented, yielding 136 UCHII region candidates throughout that galaxy. New maser detections identified two previously unknown massive YSOs. No methanol masers were detected, consistent with previous studies and supporting the hypothesis that the LMC may be deficient in these molecules. These discoveries contribute to the history of star formation in the LMC, which will lead to a better understanding of star formation in the Milky Way and throughout the universe.

Keywords: H II regions, Magellanic Clouds, masers, star formation

ACKNOWLEDGMENTS

I would like to acknowledge my advisor Victor Migenes, who expressed the utmost confidence in me, dispelling much of the personal doubts in my mind. I appreciate the great lengths he went through to ensure my success.

I would like to thank my colleagues and friends Brandon Wiggins and Derek Felli, who were such a support to me and were happy to share in my research successes. I cannot say enough how much I appreciated the many hours spent in stimulating conversation.

Finally I would like to express gratitude for the undying patience and sacrifices of my dear wife Elizabeth. She has been my stalwart support in all my undertakings, and I treasure her love above anything in this world.

Contents

List of Figures

List of Tables

Chapter 1

Introduction

1.1 Massive Star Formation

Most of the baryonic matter in the universe is tied up in stars. Without understanding stars, we wouldn't know much of anything outside of our solar system. Understanding the evolutionary cycle of stars is key to our understanding of the universe. Without the combined light of hundreds of billions of stars, we wouldn't even be aware that distant galaxies existed. The ability to identify stars in different stages of their lives has allowed us to determine distances to star clusters, masses of galaxies, the abundance of planets, and even the age of the universe. Even the existence of dark matter and dark energy is inferred through our understanding of the physics of stars.

Our understanding of low-mass star formation stands on relatively solid theoretical foundations (see McKee & Ostriker 2007 for a review). In summary, a dense molecular clump satisfying the Jeans criterion will collapse, form an accretion disk, and develop a bipolar jet around the young stellar object (YSO). As it finishes accreting matter it will continue to collapse until the central pressure forces the temperature to rise to the point at which hydrogen fusion can begin in the core, where it will then begin its life on the main sequence.

Our understanding of high-mass star formation is not that simple. In this dissertation and per convention, stars with enough mass to end their lives as core-collapse supernovae ($M_* \geq 8.0\ M_\odot$) are considered 'high-mass' stars. High-mass stars have difficulty forming in this fashion, because the onset of fusion occurs before they reach their final main-sequence mass. This works against monolithic accretion because of the increased radiation pressure of the star. Nevertheless, massive stars with accretion disks and bipolar outflows have been directly observed (Kraus et al. 2010). Therefore, there must be some other important physics simple models do not take into account. The review by Zinnecker & Yorke (2007) discusses three prevailing theories: monolithic collapse in cores with masses much greater than the Jeans mass, competitive accretion by many stars in a dense protocluster, and stellar mergers.

The major difficulty in understanding the process of massive star formation is a lack of observational data on these stars as YSOs. There are several reasons contributing to this. First of all, high-mass stars are rare compared to their low-mass counterparts. This is easily seen in the function $\xi(M)$, known as the initial mass function (IMF), which describes the distribution of stellar masses that form from a molecular cloud. The well known IMF by Salpeter (1955) suggests that $\xi(M) \propto M^{-2.35}$ clearly illustrating the drop in the number of stars at high stellar masses. Second, given their greater masses, their increased luminosities shrink their evolutionary timescales dramatically. This compounds the problem with their low numbers, because finding high-mass stars as massive YSOs is even more rare, particularly given the formation timescale of $t_{\rm form} \sim 10^5$ years vs. $t_{\rm form} \sim 10^7$ years for solar-mass stars (McKee & Ostriker 2007). Given their rarity, this puts them statistically at large distances, where resolving the individual stellar system becomes an issue. The one observational advantage massive stars have is a high luminosity, but unfortunately this is mitigated by an optically-thick dust cocoon that enshrouds most YSOs. Therefore, most of the observational work on massive YSOs is carried out at infrared and radio frequencies.

Despite their low numbers, it is high-mass stars that do most of the work in galaxies. They

provide the lion's share of the luminosity of the galaxy, particularly the ionizing radiation. For example, a 34 $M_{\odot}$ star would provide over 10^5 $L_{\odot}$ with the peak of the energy distribution occuring at ultraviolet (UV) wavelengths (Crowther 2005). Their immense stellar winds and explosive deaths (i.e. as supernovae) provide the interstellar medium (ISM) with heavy elements and mechanical energy that drives the chemical and dynamical evolution of their host galaxies. Some instances have been seen where supernova shock waves and even stellar winds have sufficiently compressed the ISM to induce future generations of star formation (Dunne et al. 2001; Elmegreen & Lada 1977). Given the key role they play in galactic evolution, the issue of exactly how massive stars form is one of the outstanding problems in astronomy.

1.2 The Large Magellanic Cloud

Visible to the unaided eye in the southern hemisphere, the Large Magellanic Cloud (LMC) is an irregular dwarf galaxy that orbits the Milky Way. Although it has on order of 100 times less mass than the Milky Way (Alves 2004), it is the fourth most massive galaxy in the Local Group. Positioned at a mere 50 kpc away, the LMC spans approximately 10° x 10° on the celestial sphere. Figure 1.1 is an optical image of the LMC and Figure 1.2 is an Hα map of the LMC, showing the prominent star-forming regions.

The characteristics of the LMC make it a prime target for observing massive star formation in a galaxy. The star-forming regions of the Milky Way are concentrated in the narrow plane of the Galactic disk. Therefore, because of our position in the Milky Way, dust extinction and source confusion prove to be a hinderance in determining the distribution of massive star-forming regions. Distance determinations based on stellar luminosities suffer from poorly-constrained extinction along the line-of-sight. Kinematic distances suffer from a near/far ambiguity in the inner galaxy. The distribution of spiral arms in the Milky Way remains largely unknown even today because the

Figure 1.1 Optical image of the LMC. Image credit and copyright: Robert Gendler (used by permission).

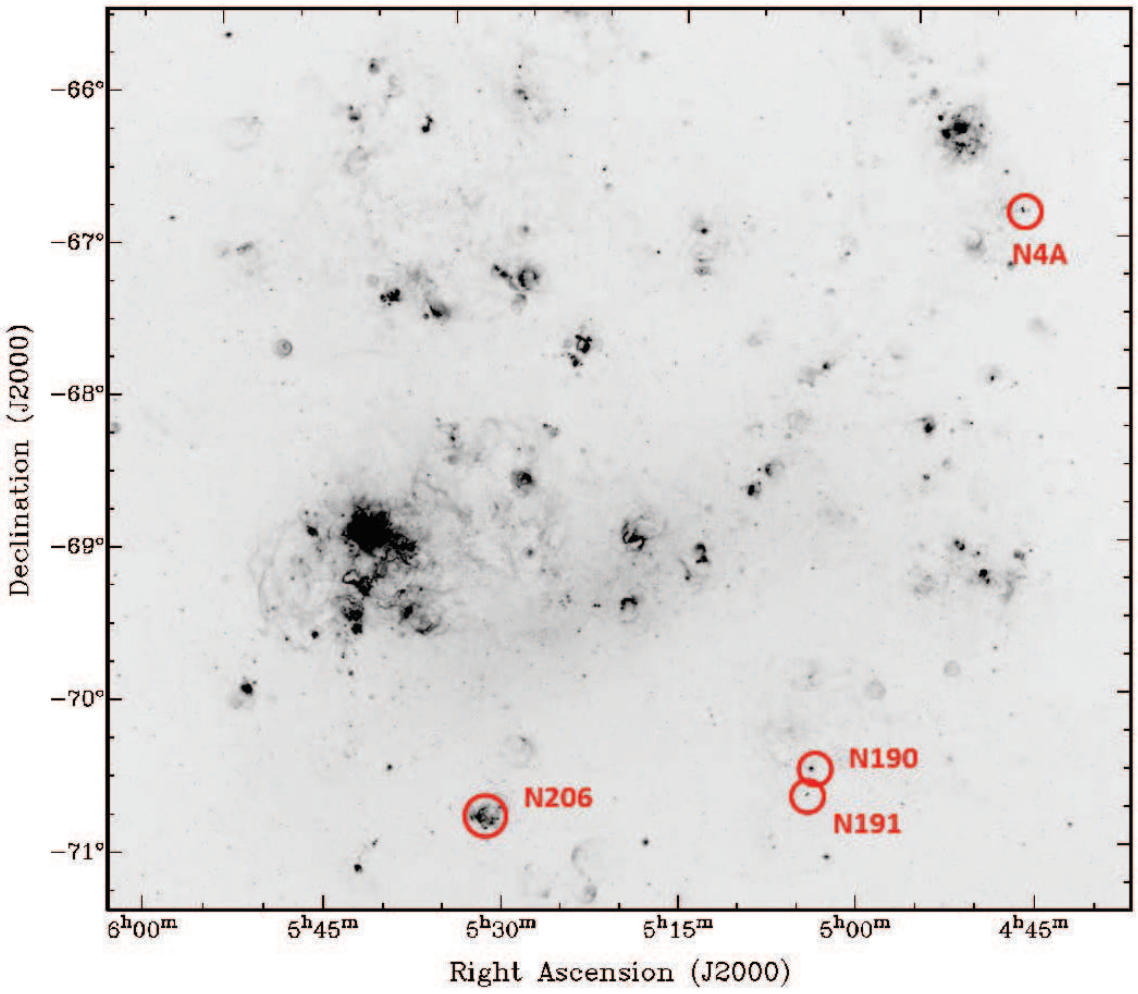

Figure 1.2 MCELS Hα map of the LMC (Smith & MCELS Team 1998). The red circles indicate the observed star-forming regions, N4A, N190, N191, and N206.

errors in distance from these effects average ∼40% (Reid et al. 2009). Given its proximity, low inclination angle, and position out of the plane of the Galaxy, the LMC gives us a favorable view of its star-forming activities. In an analogous way for stars in clusters, relative to the Sun, all the stars in the LMC are approximately equidistant. This allows us to compare relative luminosities of objects without having to worry about large distance uncertainties. In summary, the LMC provides a way for us to study star formation close up on a galactic scale.

It is important to note that the physical characteristics of the LMC and its ISM differ significantly from the Milky Way. For example, the metallicity of the LMC is lower than that of the Milky Way (Meixner et al. 2006), and the lack of a concentrated, dust-heavy disk has given the LMC a large, ambient UV field. Most of the star formation in the Milky Way occurs in its spiral arms, while the LMC lacks spiral structure. The star formation rate in the LMC is 0.2 $M_{\odot}$ yr^{-1} (Harris & Zaritsky 2009), and in the Milky Way it is ∼1.0 $M_{\odot}$ yr^{-1} (Robitaille et al. 2010). Because it is 100 times less massive than the Milky Way, the overall star formation rate per unit mass in the LMC is somewhat surprisingly higher than that of the Milky Way and even contains the most active star-forming region in the local universe (30 Doradus). It is hypothesized that tidal interactions with the Small Magellanic Cloud may have induced some of the star formation (Harris & Zaritsky 2009). Doubtless these properties will affect the galactic star formation in the LMC, and this can be advantageous because these differences are viewed in the context of the galaxy as a whole. This point of view can teach us about the physics necessary for star formation in an environment different than the Milky Way.

1.2.1 SAGE

One of the major efforts to understand the star formation process in the LMC is the *Spitzer Space Telescope* Surveying the Agents of a Galaxy's Evolution (SAGE) program (Meixner et al. 2006). They used the Infrared Array Camera (IRAC) and the Multiband Imaging Photometer (MIPS) to

survey the LMC in the mid-infrared (3.6, 4.5, 5.8, 8.0 μm) and the far-infrared (24, 70, 160 μm) respectively, since interstellar dust and young stars are some of the predominant objects at these wavelengths. Although massive YSOs are obscured at optical wavelengths, the surrounding dust absorbs the stellar radiation and reemits it in the infrared. Massive YSOs with a large UV flux are particularly bright in the infrared. Thus, the infrared light serves as a probe of the UV flux of the YSO, and can give us properties such as the mass and luminosity of the central source.

Several groups have taken advantage of the SAGE dataset, including one particular group who meticulously produced a list of 855 high-probability massive YSO candidates (Gruendl & Chu 2009, hereafter GC09). They made an initial cut in IRAC color-magnitude space of $[4.5]-[8.0] > 2.0$ and $[8.0] > 14-([4.5]-[8.0])$. They then looked at the morphology, local environment, and spectral energy distribution (SED) of this initial sample of sources to identify massive YSOs. Ellingsen et al. (2010) found the GC09 YSO candidate list to be more successful than lists compiled by other groups at identifying YSOs. Seale et al. (2009) looked at the mid-infrared spectra of almost 300 of the GC09 sources and estimated that over 95% of the GC09 list are bona fide YSOs. I therefore have adopted the GC09 list for my observations and analysis.

1.3 Radio Emission

A useful complement to the infrared observations of the SAGE survey is to look for any corresponding radio emission toward SAGE sources. Radio observations can provide additional insight to the physical processes associated with a particular infrared source. Massive YSOs often at certain stages in their evolution exhibit bright, compact radio emission that can be observed at great distances, even through the obscuring dust clouds that hide them in the visible. Thus, associated radio emission can provide strong evidence supporting the classification of massive YSOs, as well as identify sources with no emission at other wavelengths. Some of the relevant sources of radio

emission are addressed here.

1.3.1 H II Regions

Hydrogen is ionized (represented as H II) when a photon with energy greater than 13.6 eV unbinds the electron from the atom. In the vicinity of high-mass stars, large amounts of UV radiation tend to ionize the surrounding hydrogen in the ISM, creating an H II region. Within an ionization-bounded H II region, the ionization and recombination rates are in equilibrium. Free electrons in the vicinity of an ion will feel a Coulomb attraction and will accelerate, thereby emitting a photon. The distribution of frequencies depends on the electron temperature, and is thus a type of thermal emission. At electron temperatures typical of H II regions ($T_e \sim 7,500 - 10,000K$) the free-free emission will peak in the radio.

High-mass O and B stars will produce large H II regions as they live out their main sequence lives. Initially, the radio emission from these H II regions becomes detectable while the massive star is still a dust-enshrouded YSO. Given their characteristically small sizes (≤ 0.1 pc) and high densities ($\geq 10^4$ cm^{-3}), these are called ultracompact H II (UCHII) regions (Wood & Churchwell 1989a). At the distance of the LMC, the $1.5''$ resolution of the ATCA corresponds to a linear scale of 0.35 pc. Since classical UCHII regions are always point-sources at the distance of the LMC, I define an unresolved or slightly-resolved H II region associated with a massive YSO as an UCHII region.

1.3.2 Masers

Some massive YSOs during certain stages of their evolution can exhibit strong radio emission from molecular masers. A maser is analogous to the more familiar laser, and the term originally was an acronym for microwave amplification by stimulated emission of radiation. Astrophysical masers therefore describe regions of molecular gas that emit coherent beams of microwave or radio

radiation via stimulated emission. The relative populations of two energy states ($n_1, n_2, n_2 > n_1$) in a gas is related by the Boltzmann distribution

$$\frac{n_2}{n_1} = e^{\frac{-\Delta E_{12}}{k_b T_{ex}}} \tag{1.1}$$

where $-\Delta E_{12}$ is the energy difference between the two levels, k_b is the Boltzmann constant, and T_{ex} is the excitation temperature. For systems in local thermodynamic equilibrium (LTE), the excitation temperature is equal to the regular thermal temperature, and in general the population of the lower energy state is greater than the upper energy state. If the gas is subject to an environment where the local conditions cause an upper state to be filled more rapidly than the spontaneous deexcitation rate, then this can lead to a situation known as a population inversion. This can occur when the upper state is metastable, such as when a so-called 'forbidden' transition is involved. Equation 1.1 implies that such a gas would have a negative T_{ex}, obviously indicating a breakdown of LTE. The process responsible for creating the population inversion is known as the 'pumping' mechanism. Such processes are usually complicated involving multiple transitions among several energy levels.

Astrophysical masers can occur when there is a population inversion between two rotational energy levels in a molecule. A metastable upper state can have a relatively long spontaneous transition lifetime. However, a downward transition can also be induced or 'stimulated' from an incident photon with the same energy as the transition. This transition emits a photon which adds itself with the same phase and direction to the radiation field that induced its transition. This behavior is due to the fact that photons are integer spin particles, and therefore follow Bose-Einstein statistics. This additional photon can now interact with a neighboring molecule, which can in turn stimulate another transition. This leads to a chain reaction through the molecular gas releasing an exponentially increasing number of coherent photons. Astrophysical masers are therefore very compact and intense, and thus serve as excellent probes of gas structure and kinematics.

H_2O **Masers** There are three maser species that are particularly bright and associated with star formation. The brightest maser transition is the 22.2 GHz transition of water. This energy corresponds to the $6_{16} \rightarrow 5_{23}$ rotational transition, where the first number is the total angular momentum quantum number and the subscripts are the projections of the angular momentum onto the molecular rotation axes. Water masers are often associated with UCHII regions and thus serve as useful indicators of massive star formation (Churchwell 2002, p. 50). The 22.2 GHz water maser pumping mechanism is thought to predominantly arise from collisions with H_2 in high-density regions. These high densities arise at shock fronts between bipolar outflows from massive YSOs and the ambient ISM. Given their brightness and compact size, water masers make excellent tracers of the molecular gas around these massive YSOs and have been used for high-resolution proper motion and parallax studies (e.g. Goddi et al. 2011).

CH_3OH **Masers** The 6.7 GHz ($5_1 \rightarrow 6_0$ A^+) maser transition of methanol (CH_3OH) is the second brightest known astrophysical maser, yet has only been discovered relatively recently (Menten 1991). This maser transition has been found to be almost exclusively associated with massive YSOs (Breen et al. 2013), and have become a useful tool in the study of massive star formation. They are radiatively pumped by intense infrared emission from hot dust being heated by the intense UV radiation field of a massive YSO. High-resolution studies of methanol masers have shown that they often trace ring-like structures seen in infall or in outflow (Bartkiewicz et al. 2009). They typically appear at some of the earliest stages of massive star formation, during aggressive accretion before the onset of nuclear fusion in the stellar core. If there is a 6.7 GHz methanol maser, there is a massive YSO associated with it.

OH **Masers** The hydroxyl radical (OH) was the first maser discovered (Weaver et al. 1965). The ground state of OH has four hyperfine structure lines corresponding to interaction between the angular momentum of the system and the nuclear spin. F is a quantum number corresponding to

the total angular momentum which includes the contribution of the nuclear spin. The main lines correspond to $\Delta F = 0$ transitions and are at 1665 and 1667 MHz. The satellite lines correspond to $\Delta F = 1$ transitions and are at 1612 and 1720 MHz. OH masers are found in a variety of different astrophysical environments. They can be seen in atmospheres of late-type stars, supernova remnants, star forming regions, in external galaxies and even in comets. For star formation, they are often found toward UCHII regions, situated outside the ionization front (Churchwell 2002, p. 50). The 1665 MHz and 1667 MHz lines are also associated with protostellar disks and are radiatively pumped, and in such instances are often correlated with 6.7 GHz methanol masers.

1.3.3 Other Sources

In addition to massive YSOs, several other astrophysical sources emit radio waves, such as pulsars, supernova remnants, and planetary nebulae. It is likely that a given field of view would be contaminated by a number of these sources. Some of the strongest radio signals come from active galactic nuclei (AGNs). The source of AGN emission is from a central supermassive black hole currently accreting matter. In the radio, the emission is primarily synchrotron in nature, produced when high-velocity electrons spiral around the intense magnetic field lines around the black hole. The synchrotron emission is nonthermal and has a power spectrum that decreases rapidly with increasing frequency. Differentiating different unresolved nonthermal sources based on the spectral index alone is not usually possible, thus additional multi-frequency observations are usually needed. For the case of AGNs, they are often associated with bright mid- and far-infrared emission (Sanders 1999) and can even be identified by their IRAC colors (Stern et al. 2005).

1.4 Purpose

Although the entire LMC has been observed at radio frequencies (see Section 3.2), there is still a need for detailed, high-resolution work to investigate individual sources, in addition to a wide view of the galaxy. Even though the large scale radio emission can be matched with the large scale infrared emission, a one-to-one comparison of individual sources still needs to be completed. It would be an unrealistic use of telescope time to survey such a large area of the sky at high-sensitivity and resolution, but sometimes the significance of such observations is undervalued. Just as much about star formation can be learned from a handful of well-studied sources as a whole ensemble of objects in a galaxy. If the pertinent objects of interest from a global study could be extracted, then the high-resolution and superior sensitivity observations could be targeted toward those sources. Instead of having to search the entire LMC at high resolution, just the massive YSOs can be targeted to learn about massive star formation in the galaxy as a whole. High-resolution radio data can be combined with the SAGE survey in order to give theorists a setting of massive star formation in the context of the LMC. If the current state of star formation in the LMC is understood, astronomers will be able to better understand star formation in the Milky Way. This knowledge could then extend to the more distant galaxies where resolving individual star-forming regions is problamatic. We would then have a better grasp on the formation history and evolution of the universe.

My dissertation consists of high-quality observations toward certain lesser-known star-forming regions in the LMC for radio emission associated with GC09 massive YSO candidates. I observed for both radio continuum emission from compact H II regions and spectral line emission from masers toward the GC09 candidates. Detections are strong indicators that the candidates are bona fide YSOs. The mid-infrared properties of UCHII regions observed in this work and elsewhere were examined to see if there were some simple IRAC color-magnitude criteria that could be utilized to identify UCHII regions in the LMC. The SEDs in the radio and infrared were examined

to determine a plausible stellar spectral type for the YSOs. Other extraneous radio emission is reported and the possible nature of these sources is discussed.

Chapter 2

Observations and Data Reduction

2.1 Radio Interferometry

The angular resolution of a telescope depends on the size of the telescope and the observed wavelength of radiation. Although it is easy to build radio dishes a factor of 100 times larger than optical telescopes, this does not make up for the factor of more than 10,000 times longer wavelengths. To overcome this deficiency, radio interferometry can be used to obtain the resolution of a dish the same size as the separation between its two most distant elements. This process is called aperture synthesis interferometry. The fundamental unit in an interferometer is the baseline, the vector connecting a pair of telescopes. The more independent baselines in an interferometer, the better it can image a source on the sky.

Consider the two-element interferometer in Figure 2.1. Let **b** be the baseline separation vector, and let $\hat{\mathbf{s}}$ be a unit vector pointing toward a radio source at an angle θ from the horizontal. An incoming plane wave will reach the antenna on the left at a time $\tau = \frac{b\cos\theta}{c}$ after it reaches the antenna on the right. The two voltages produced by the radio wave are then sent to a correlator which multiplies and time-averages the signals together. The correlator outputs a complex number

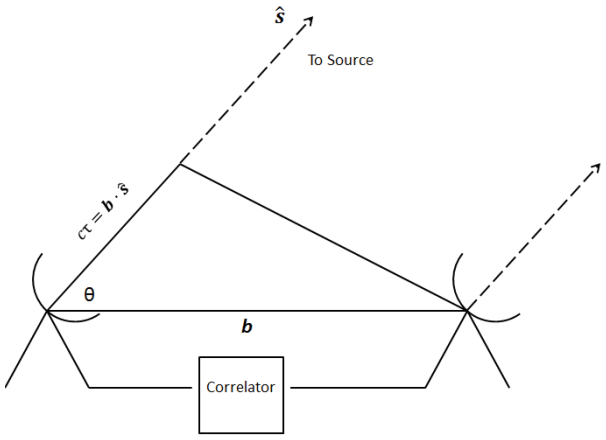

Figure 2.1 Schematic of a simple two-element interferometer.

known as a visibility, whose amplitude depends on the source brightness and whose phase depends on the signal delay. The total visibilities from all the baselines in the array build up what is known as the spatial coherence function V, which is related to the intensity $I(s)$ of the source by

$$V = \iint_{\Omega} I(s) e^{2\pi i b \cos\theta} d\Omega \tag{2.1}$$

where $d\Omega$ is the solid angle of the source on the sky. Thus, $I(s)$ can be recovered from the Fourier transform of the spatial coherence function V. The greater the number of baselines with a variety of geometries with respect to the source, the better the interferometer can probe the Fourier space and therefore produce a more accurate image.

2.2 The Australia Telescope Compact Array

The prime radio interferometer with a view of the southern sky is the Australia Telescope Compact Array (ATCA, see Figure 2.2). The array consists of five antennas that primarily lie along a 3 km linear track in the east-west direction, and an additional antenna stationed another 3 km away, giving the interferometer a total length of up to 6 km. The angular resolution of a radio interferometer is on the order of $\frac{\lambda}{b}$ where λ is the observed wavelength and b the baseline separation between

Figure 2.2 Five of the antennas of the ATCA. Credit: CSIRO

the most distant elements of the array. For observations at 6 cm, the ATCA has a resolution of $\sim 2''$. However, since the array elements are linear, the resolution is only good in one direction. In order to accurately map the image in the other directions, observations span a long enough time for the rotation of the Earth to reorient the source in the sky with respect to the array, a process known as Earth-rotation aperture synthesis. The components of the projection of the sky onto a particular baseline can be split into two orthogonal components, denoted u and v. Figure 2.3 shows the visibilities in the (u,v) plane for one of the observing runs. The dimensions are measured in units of the observed wavelength. The linear structure of the array and the varying projection angle due to the rotation of the Earth is apparent.

The device that correlates the signals from two antennas together on a baseline at the ATCA is called the CABB (Compact Array Broadband Backend). The CABB has two independent fre-

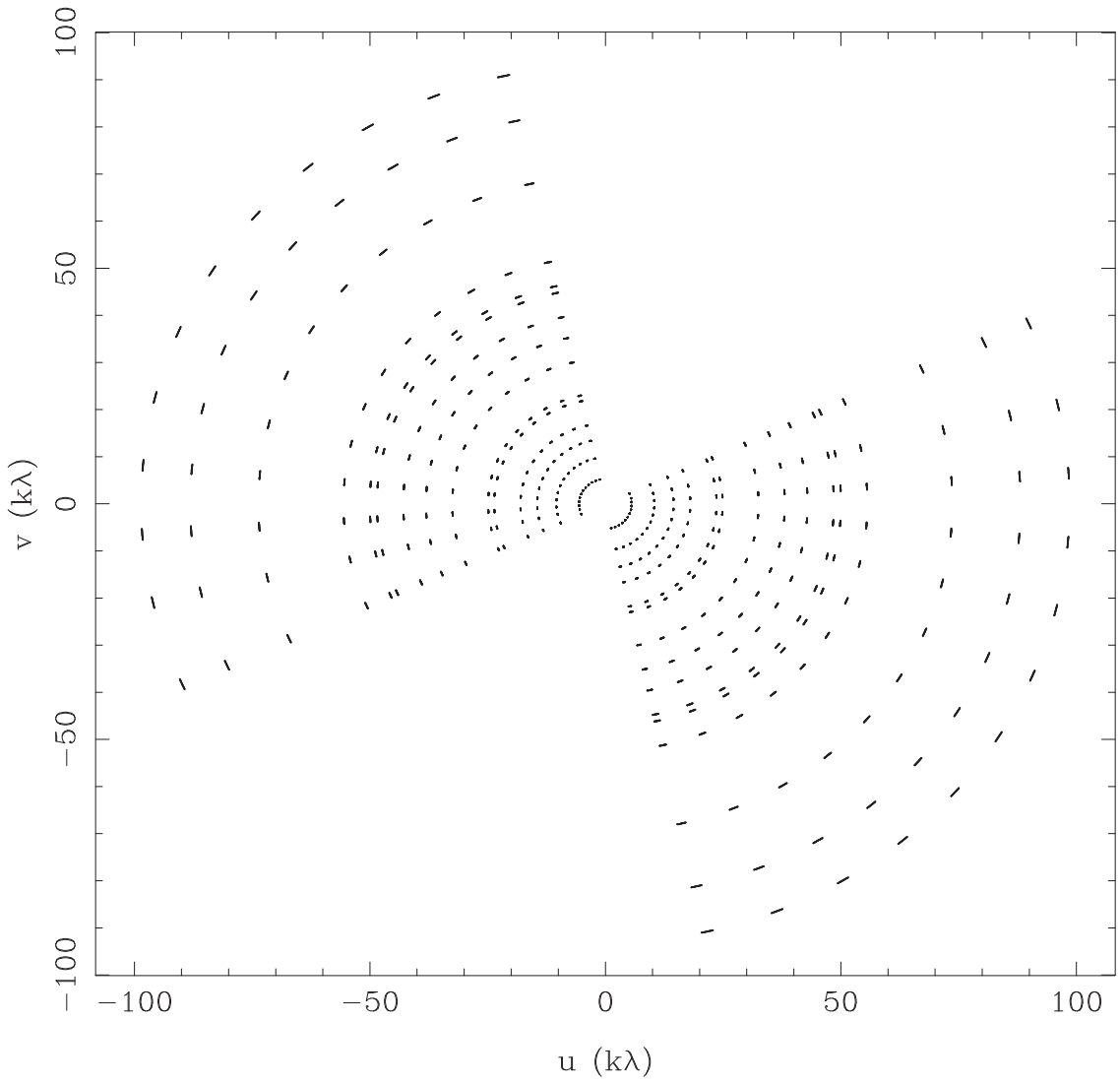

Figure 2.3 Plot of the (u,v) plane. The gaps in the curves indicate times when the telescope was observing other sources.

quency configurations (called IFs) each with a bandwidth of 2 GHz. These are analogous to filters in optical telescopes, but with the advantage of being able to be positioned at any frequency the receiver sensitivity range. The CABB also allows for high-resolution spectral line observations (called 'zoom' bands) to be positioned anywhere within the 2 GHz band in each IF. This allows the ATCA to observe broadband continuum at two different central frequencies with simultaneous spectral-line observations. The ATCA also boasts new sensitive 4 cm receivers (4.0 GHz - 10.8 GHz). With such observing versatility while pushing sensitivity limits, the ATCA is the premiere radio interferometer in the southern hemisphere.

2.3 Observations

I observed four massive star-forming regions in the LMC (N4A, N190, N191, and N206; Henize 1956) as seen in Figure 1.2. Three of these regions, (N4A, N190, and N206) were observed for the 22.2 GHz water maser line with ATCA. These observations were acquired from the archival data in the Australia Telescope Online Archive (ATOA) from 2008 March 15 (part of program CX139). The ATCA was in its 1.5 km array mode, observing at a central frequency of 22.215 GHz with a bandpass of 16 MHz divided into 512 channels. This gave each channel a spectral resolution of 31.25 kHz, corresponding to a velocity resolution of 0.422 km s^{-1}. The integration time on each source was around 20 min over the course of seven hours.

I took additional observations with the ATCA on 2013 February 9 under program number C2773. These observations investigated the N206 region in greater detail. The archival data took only one pointing toward N206, covering only a small portion of the emission region. This new data covered four additional pointings with the 6 km array. These observations were taken in an attempt to find water masers associated with GC09 massive YSOs and covered an additional 12.5 $arcmin^2$ of emission from N206 for a total of $\sim$15.5 $arcmin^2$. These observations positioned

the two IFs so that they overlapped around the central frequency of 22.200 GHz, giving a total bandwidth of 3 GHz. Since water masers often trace high velocity outflows from YSOs, a high-resolution spectral band of 16 MHz was chosen, giving a total velocity width of 228 km s^{-1} around the systemic velocity, sufficient to observe the high-velocity masers. The observations had a high spectral resolution of 0.488 kHz, or a velocity resolution of 0.007 km s^{-1}. The integration time toward each pointing was 60 min over the course of six hours.

I observed a second time with the ATCA in November of 2013. This included five pointings toward 34 GC09 massive YSOs in N190, N191, and N206. These observations looked for the 6.7 GHz maser transition of methanol, and excited OH at 6.035 GHz. They also observed for continuum emission at central frequencies of 6.0 GHz and 9.0 GHz, each with a 2 GHz bandwidth. The integration time on each source was about 70 minutes over the course of seven hours.

2.4 Data Reduction

Data reduction procedures were carried out in MIRIAD, the standard radio reduction package used with the ATCA (available at http://www.atnf.csiro.au/computing/software/miriad/). All data needed to be calibrated for amplitude, bandpass, and phase. Then the calibrated data were imaged, cleaned, self-calibrated, and finally converted into a fully reduced data product. Figure 2.4 illustrates the reduction procedure used to process the data.

2.4.1 Calibration

The absolute flux of radio observations is always determined by comparing the instrumental amplitudes to a calibrator source of known flux. The primary calibrator used for most ATCA observations is the radio galaxy PKS B1934-638, which has a well-modeled SED across the radio spectrum. A single observation of this source at the beginning of the observing is generally suffi-

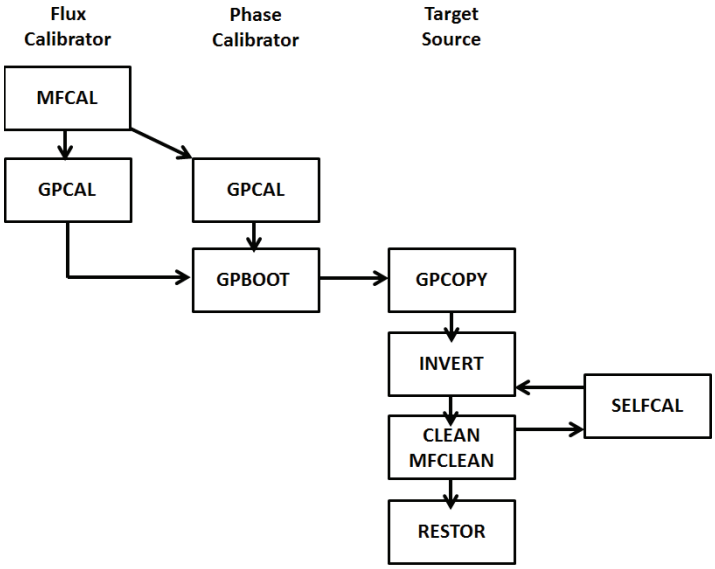

Figure 2.4 Schematic of the reduction procedure followed. Adapted from the MIRIAD User's Guide.

cient to calibrate the data to a flux accuracy of better than 10%.

Because it is a bright source, PKS B1934-638 was also used as the bandpass calibrator. Since the receivers don't respond equally to different frequencies, a strong source is needed to accurately observe how the response varies across the band. It was also used for polarization calibration, but these effects are not considered here.

A secondary calibrator known as the phase calibrator is used to probe the effects of the atmosphere throughout the duration of the observing run. These atmospheric effects are dominated by the refraction and attenuation of the radio waves by water vapor in the troposphere. The effects become more pronounced at higher frequencies, so observations of the phase calibrator need to occur more frequently. This is especially important for water maser observations, where the emission can be absorbed by the atmospheric water vapor, necessitating calibrator observations every few minutes (although those energy levels are relatively unpopulated at standard temperature and pressure). The phase calibrator also needs to be close to the observed targets, so that the same gen-

eral region of the atmosphere is being probed. These atmospheric effects on the phase calibrator are modeled and then removed from the target source data.

The MIRIAD task used to calibrate the bandpass was MFCAL. GPCAL calibrated the antenna gains. Both tasks were executed on the flux calibrator, and the bandpass correction was passed on to the secondary calibrator. Then GPCAL determined the antenna gains for the phase calibrator, which was observed during the course of the observing run. The varying antenna gains tracked the dynamic atmospheric conditions over time. The phase calibrator fluxes are arbitrary however, and thus the task GPBOOT was used to convert the relative fluxes into an absolute flux based on the flux calibrator. Then the flux amplitude, bandpass and phase calibration tables were copied to the target source data via GPCOPY, completing the primary calibration.

2.4.2 Imaging

To convert the visibilities into a sky intensity, Equation 2.1 was inverse-Fourier transformed. This was done using the INVERT task in MIRIAD. A compromise between the natural and uniform weighting schemes was used to optimize the minimization of sidelobes and to maximize point-source sensitivity. An example of such an image is shown in Figure 2.5. The strong web-like structures reflect the point spread function based on the (u,v) coverage, as can be seen in Figure 2.6. MIRIAD has a deconvolution procedure called CLEAN which removes the telescope response pattern shown in Figure 2.6 from the so-called 'dirty' map to find the point sources. This works the same for extended sources since they can be considered a collection of point sources with different intensities. Once the CLEAN procedure found all of these points, the RESTOR function was used to produce the so-called 'clean' map. The result of this process for the data in Figure 2.5 is shown in Figure 2.7.

Further improvements on image quality and sensitivity can be made through a process called self-calibration. Once a clean map is made, further improvements can be made in images con-

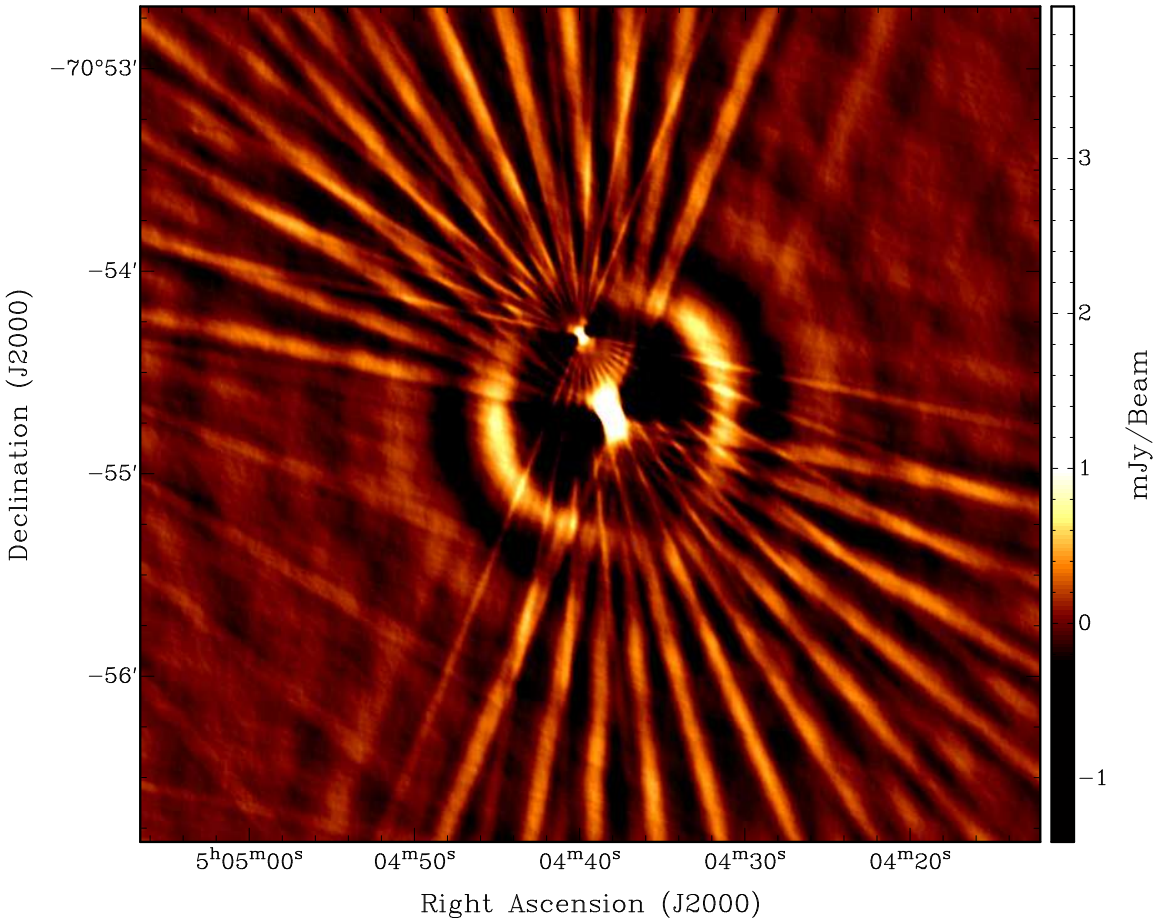

Figure 2.5 A 'dirty' radio map. The point spread function of the array is painfully apparent. The peak flux density is 3.97 mJy beam^{-1} and the rms is $\sim$150 μJy beam^{-1} in the map.

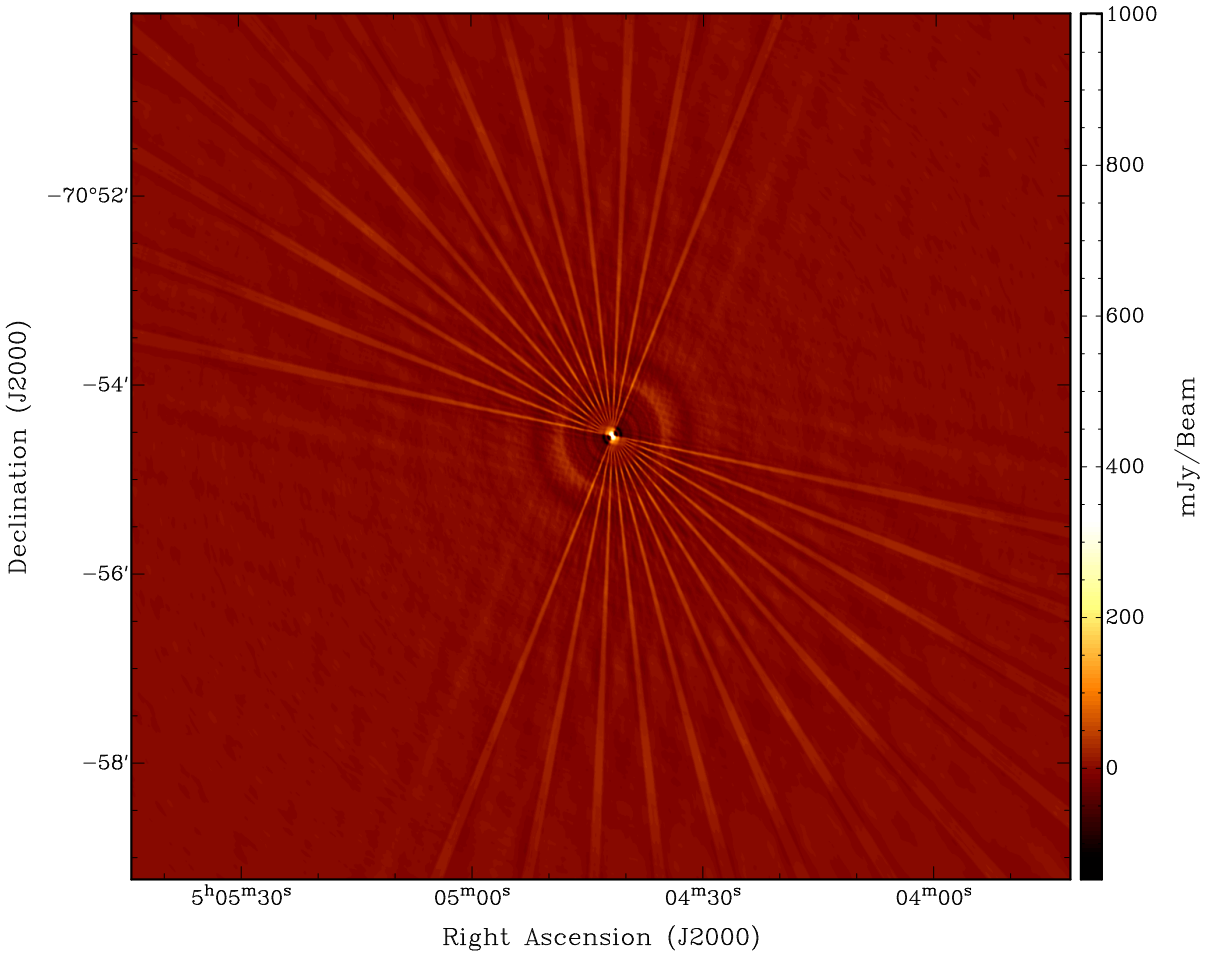

Figure 2.6 The beam pattern shows the response of the array to a point source for the given observing configuration and (u,v) coverage.

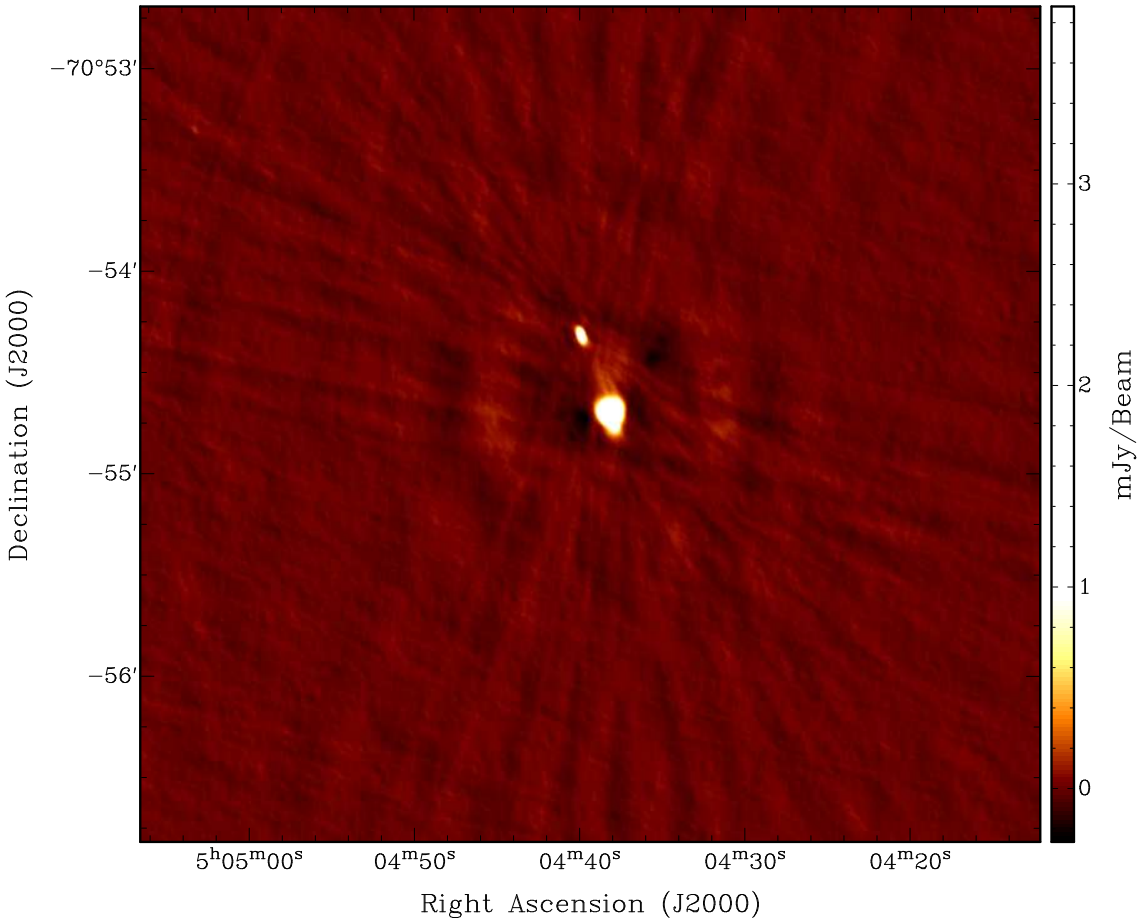

Figure 2.7 A 'clean' radio map. The array response pattern has been removed and only the source emission is left. The peak flux density is now 3.62 mJy beam^{-1} and the rms is only $\sim$22 μJy beam^{-1} in the map.

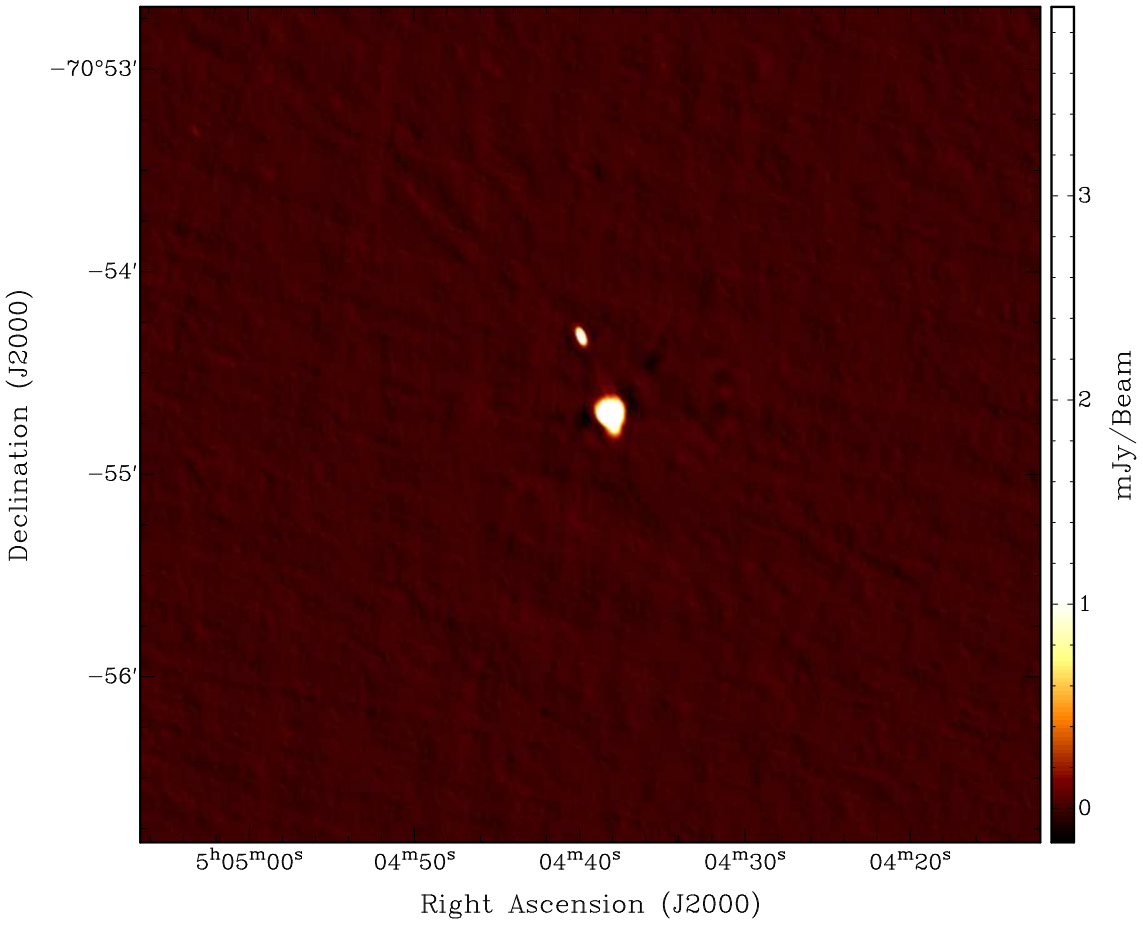

Figure 2.8 A final, self-calibrated radio map. The peak flux density is 3.60 mJy beam^{-1} and the rms is now $\sim$15 μJy beam^{-1} in the map.

taining a source with a high signal-to-noise ratio. A model of true emission in the map (usually determined by the observer) is passed along to the SELFCAL process, which improves the phase corrections for those regions in the map with emission. This was done iteratively until no further improvements in the phase can be made, and then the amplitude was corrected with the improved phases. This produced a final, self-calibrated image of the region (see Figure 2.8).

Spectral-line maps were made in a similar fashion but rather than producing a single, broadband

continuum-averaged map, an image cube was produced, with each plane of the cube representing different velocity slices across the spectrum. The doppler velocities of the masers are generally not known *a priori* and often a single maser feature will have multiple velocity components.

2.4.3 Data Products

Both my February 2013 and March 2008 archival data were reduced using standard procedures in MIRIAD. The amplitude calibrator was PKS 1934-638, and had an assumed flux of 0.84 Jy, accurate to $\sim$10%. One major exception is that for the 2013 data, PKS B1934-638 was not observable during the course of the observation. Flux calibration was thus done on a secondary calibrator, PKS B0537-441. Based on observations over the past two years, its flux at 22 GHz has had an average value of 7.5 Jy, but has varied by $\sim$25%. A similar error on the amplitude calibration for that data set is expected. Image sensitivity for the 2008 observations was $\sim$7 mJy beam^{-1} rms for N4A and N190, and $\sim$8.6 mJy beam^{-1} rms for N206. For the 2013 observations of N206, the spectral data were averaged together to a velocity resolution of 0.224 km s^{-1} to increase sensitivity. Image sensitivity in the spectral cubes was $\sim$20 mJy beam^{-1} rms and $\sim$82 μJy beam^{-1} rms in the continuum image. The resolution of the 2008 1.5 km array data were typically about 1.0$''$ and the 2013 6 km array had a resolution of about 0.5$''$.

The November 2013 data were also reduced using standard procedures. The assumed flux density of PKS B1934-638 was 4.5 Jy at 6 GHz and 2.7 Jy at 9 GHz and was accurate to $\sim$5%. Continuum image sensitivity was $\sim$20 μJy beam^{-1} at 6 GHz and $\sim$30 μJy beam^{-1} at 9 GHz. Maser spectral cube sensitivity was $\sim$8 mJy beam^{-1} rms. The resolution of the images was 1.5$''$ at both frequencies, which is close to the *Spitzer* IRAC resolution of 2$''$, allowing for better comparison between maps.

Chapter 3

Results

3.1 Masers

A total of four 22.2 GHz water masers toward two high-mass star-forming regions were detected. Four maser spots were detected toward N4A and two were detected toward N190. The integrated flux toward the masers in N4A as a function of velocity are displayed in Figure 3.1. The two masers in N190 are displayed in Figure 3.2.

Maser positions and peak flux densities were determined by the MIRIAD task IMFIT, which fits two-dimensional Gaussians to the sources. Their positions, properties and any associated GC09 YSO or 2MASS point source (Two Micron All-Sky Survey, Cutri et al. 2003) are reported in Table 3.1. A maser is considered to be associated with a YSO if it is located within $2''$ of the YSO (i.e. the resolution of both the *Spitzer* SAGE survey used by GC09 and 2MASS) after the practice of Ellingsen et al. (2010).

No 6.7 GHz methanol or 6.035 GHz excited OH masers were detected down to a 3σ of $\sim$24 mJy beam^{-1} rms in the unaveraged spectral channel clean maps. This result is consistent with previous maser surveys of the LMC and supports the hypothesis that the underabundance of

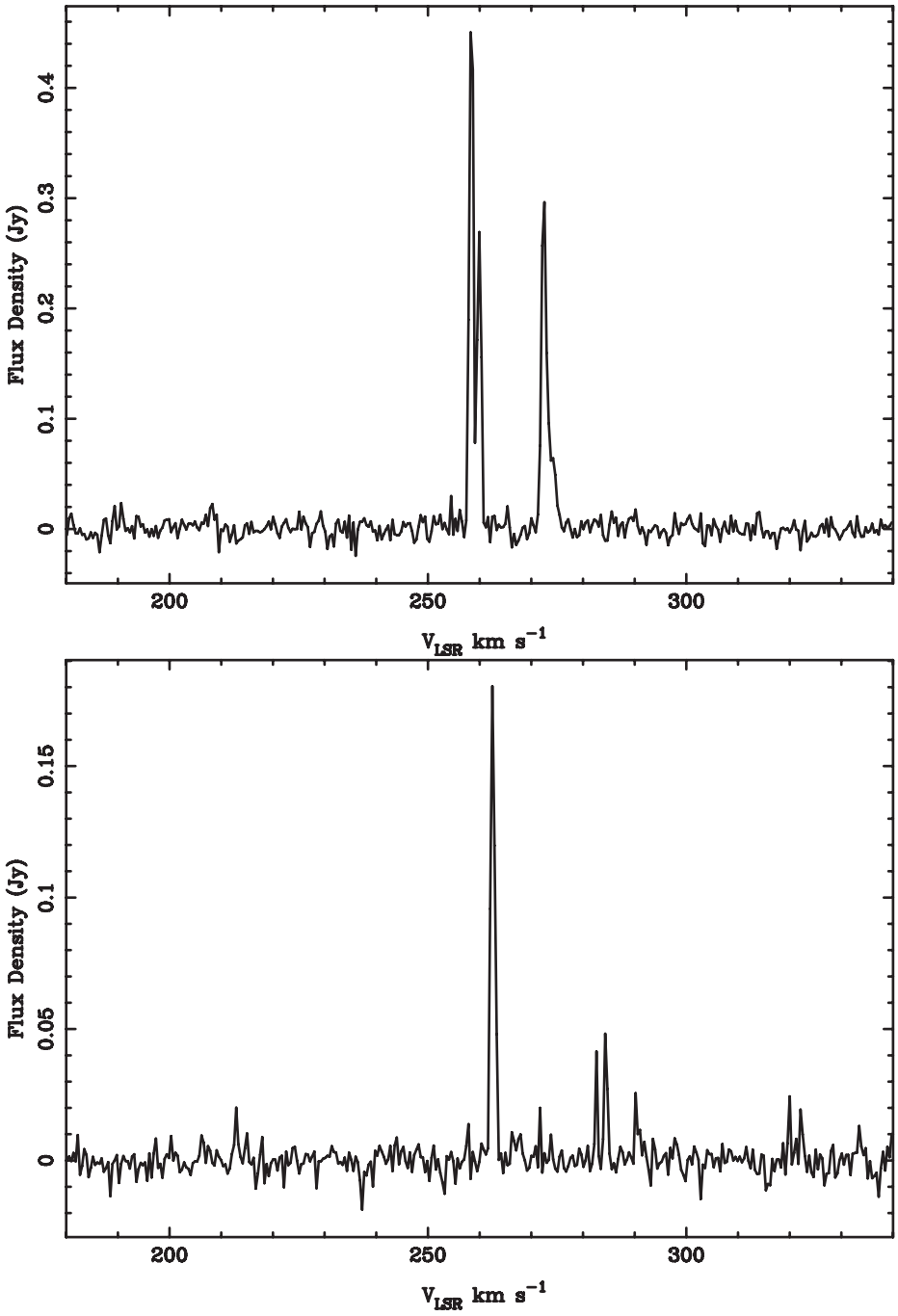

Figure 3.1 Spectra of the 22.2 GHz water masers toward N4A. *Top*: The three peaks of maser spots associated with the GC09 massive YSO. *Bottom*: The maser spot associated with the diffuse filamentary emission. Note that the two small peaks around 283 km s^{-1} are spurious signals due to an incomplete sampling of the uv plane.

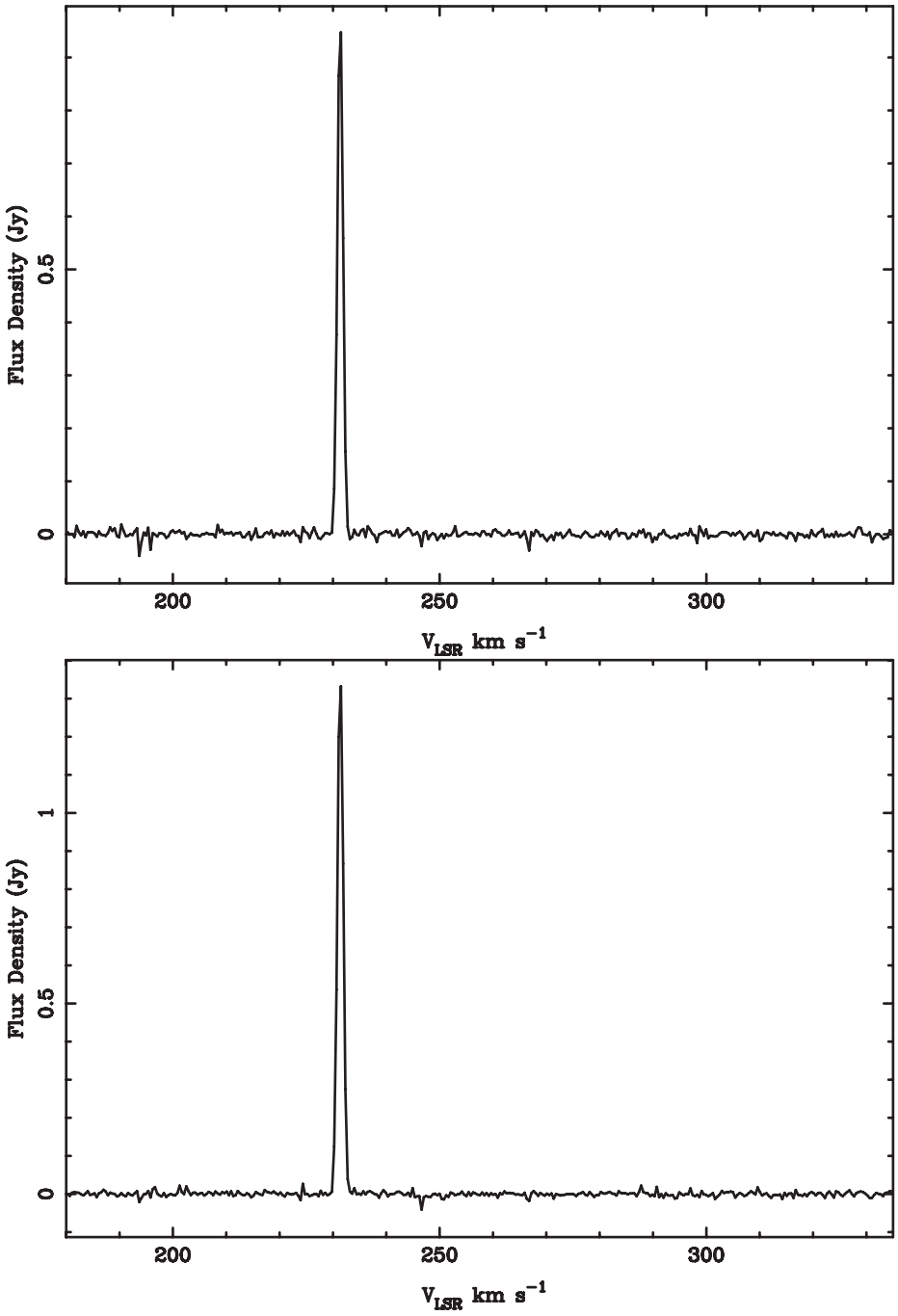

Figure 3.2 Spectra of the 22.2 GHz water masers toward N190. *Top*: The maser associated with 2MASS J05042500-7043444. *Bottom*: The maser associated with 2MASS J05042559-7043434.

Table 3.1. Detected H_2O Masers

Source	RA (J2000) h m s	Dec (J2000) ° ′ ″	S_{max}[a] mJy beam^{-1}	Velocity km s^{-1}	Δ V (FWHM) km s^{-1}	Associations
N4A-M1	04 52 05.24	-66 55 13.9	230±15	262.5	1.0	J045205.39-665513.8[b]
N4A-M2	04 52 09.05	-66 55 22.5	261±10	259.9	1.0	J045209.22-665521.9[c,d]
N4A-M3	04 52 09.07	-66 55 22.6	431±30	258.4	1.0	J045209.22-665521.9[c,d]
N4A-M4	04 52 09.21	-66 55 22.2	275±24	272.5	1.1	J045209.22-665521.9[c,d]
N190-M1	05 04 24.98	-70 43 42.9	1271±132	231.5	1.3	J050424.82-704343.7[c] J05042500-7043444[e]
N190-M2	05 04 25.44	-70 43 41.6	1615±159	231.5	1.3	J05042559-7043434[e]

Note. — Masers detected in this work. The 2nd and 3rd columns list the positions of the individual maser spots. The 5th and 6th columns give the peak velocity and the FWHM of the best-fit gaussian to the feature. The last column gives the relevant associations with the maser spot.

[a]Peak flux density.

[b]Gruendl & Chu (2009) diffuse source.

[c]Gruendl & Chu (2009) massive YSO.

[d]Contursi et al. (2007) Star 2.

[e]Cutri et al. (2003) 2MASS point source.

masers in the LMC may be in part due to the lower metallicity environment (Green et al. 2008).

3.2 Compact H II Regions

Eight compact H II regions were detected at both 6 GHz and 9 GHz, and one of these was detected at 22 GHz as well. Although the entire LMC has been imaged in the radio at 843 MHz by the Sydney University Molonglo Sky Survey (SUMSS, Bock et al. 1999), and at 4.8 GHz and 8.6 GHz by Dickel et al. (2005), half of these sources were detected for the first time here. Indebetouw et al. (2004) surveyed parts of the LMC with the ATCA at 4.8 GHz and 8.6 GHz, including N206 at a similar resolution of this survey, but with inferior sensitivity. The positions and flux densities of all eight detected compact H II regions are listed in Table 3.2.

Four of these sources are classified as UCHII regions. The UCHII regions were identified by two criteria. First, by their association with known massive YSOs and second, by the spectral index at the observed frequencies. The spectral energy distribution is assumed to follow a power-law in the form of $S \propto \nu^{\alpha}$. Thermal radio sources are expected to have spectral indices ranging from $\alpha \sim +2$ (for optically thick sources) down to slightly negative values (around $\alpha \sim -0.1$ for optically thin sources). All sources have spectral indices consistent with thermal emission and their values are listed in Table 3.2.

The presence of an UCHII region with a massive YSO gives us information about the evolutionary stage of the YSO and the UV flux being emitted. Knowing the number of ionizing photons creating an UCHII region gives a measure of the mass (and thus spectral type) of the young star. The spectral type of each ionizing star was determined based on the radio flux density at 6 GHz, which is directly related to the number of ionizing Lyman continuum photons. For a given electron temperature, the number of ionizing photons can be calculated. If the bulk of the UV flux is assumed to come from a single star, then the spectral type of that star can be determined. There are doubtless multiple stars in these OB associations, but the difference in flux between spectral types is so great that the approximation is valid for the accuracy warranted by the data. The number of

ionizing photons Q has been calculated from Equation 5 in Martín-Hernández et al. (2003),

$$Q = 4.634 \text{ x } 10^{46} \left(\frac{T_e}{10^4 K}\right)^{-0.45} \left(\frac{\nu_{GHz}}{5\ GHz}\right) \left(\frac{R}{1\ kpc}\right)^2 \left(\frac{S_\nu}{1\ Jy}\right) a_\nu^{-1} \tag{3.1}$$

where T_e is the electron temperature, taken to be 7,500 K after the manner of Martín-Hernández et al. (2003), ν the observed frequency, R the distance to the source, taken to be 50 kpc after Alves (2004), S_ν the flux density in Jy, and a_ν^{-1} a correction factor of order unity, taken to be 0.986 after Mezger & Henderson (1967). The spectral type was determined based on the theoretical mass-radius relationship models presented in Table 1 of Crowther (2005). These results are also listed in Table 3.2.

Another way to estimate the spectral type of the ionizing star for the UCHII regions is to model the massive YSO based on the infrared SED. I used the online model fitter developed by Robitaille et al. (2007), which fits an input SED from a source to a precalculated set of 200,000 YSOs with varying physical parameters, such as mass, stellar radius, temperature, accretion rate, and viewing angle (Robitaille et al. 2006). My input SEDs came from the optical data from the Magellanic Clouds Photometric Survey (Zaritsky et al. 2004), near-infrared data from 2MASS, and the mid-IR photometry from GC09. Sources were matched with optical and near-infrared counterparts if they were separated by less than $1.5''$. The best-fit model from the Robitaille et al. (2007) fitter was used to obtain an estimate of the total luminosity of the central YSO. This was used to determine a spectral type based on the same models from Crowther (2005). These are also listed in Table 3.2.

Discrepancies between the determined spectral type from the radio data and the infrared data can arise from several factors. The primary reason would be that the radio and infrared both compete for the UV photons. In general, the younger the YSO, the more dust and the brighter the infrared emission, whereas the more evolved YSO will eventually photodissociate the surrounding dust and the infrared emission should fade away as it evolves into a classical H II region. I analyzed each of the massive YSOs with UCHII regions individually, but the analysis may be flawed due to the other uncertainties. First, my assumption that the bulk of the ionizing radiation is provided by

Table 3.2. Compact H II Regions at 6 and 9 GHz

Source	RA (J2000)	Dec (J2000)	$S_{6\ GHz}$[a]	$S_{9\ GHz}$	α	log Q	Spectral Type	
	h m s	° ′ ″	mJy	mJy		s^{-1}	Radio	Infrared
N190-HII1[b]	05 04 25.5	-70 43 44	2.56±0.21	4.39±0.34	1.3	47.54	B0V	
N191-HII1[b]	05 04 38.1	-70 54 42	24.7±1.4	24.9±1.3	0.0	48.53	O8V	
N191-HII2[c]	05 04 39.9	-70 54 19	3.39±0.18	3.20±0.18	-0.1	47.66	B0V	O9.5V
N206-HII1[b,c,d]	05 30 20.3	-71 07 49	3.92±0.25	3.35±0.19	0.2	47.73	O9.5V	B1.5V
N206-HII2[b,c]	05 30 20.6	-71 07 39	7.84±0.51	7.14±0.41	-0.2	48.03	O9V	B1V
N206-HII3[b]	05 30 47.7	-71 07 56	0.20±0.03	0.18±0.02	-0.2	46.44	B1V	
N206-HII4[b]	05 30 56.3	-71 06 02	4.95±0.31	4.61±0.34	-0.2	47.83	O9.5V	
N206-HII5[b,c]	05 31 22.9	-71 04 10	2.79±0.25	2.61±0.20	-0.2	47.58	B0V	B0.5V

Note. — Compact H II regions detected in this work. The spectral type is determined by the tables in Crowther (2005).

[a] S_ν indicates the integrated flux density at frequency ν.

[b] Source is resolved with the ATCA synthesized beam.

[c] Indicates an UCHII region.

[d] Source has a 22 GHz $S_{22\ GHz}$ of 636 μJy.

one star may not be a valid approximation. Second, there could be two different stars, one with an optically thin envelope and the other with an optically thick, and the bulk of the radio and infrared may come from different sources. Another possibility, as discussed before, is that the exact mechanisms of massive star formation are not well understood, and disk-envelope models of Robitaille et al. (2007) may be invalid. Secondary sources of error would come from the assumption of a spherically symmetric, homogenous, ionization bounded H II region, and from the electron temperature assumption (although from Equation 3.1 the value Q depends weakly on the electron temperature). Despite all of these caveats, there is still reasonable agreement between the the radio and infrared spectral types.

3.2.1 Mid-Infrared Colors of UCHII Regions

Historically, the study of UCHII regions has been primarily confined to the Milky Way. Indebetouw et al. (2004) targeted Wood & Churchwell (1989b) IRAS sources in the LMC to find UCHII regions. The difference between the resolution of the ATCA and IRAS caused problems with proper source association and in some cases misidentification. The IRAC bands from the *Spitzer* SAGE program provides an infrared map of the entire LMC with resolution similar to the ATCA. This allows for radio sources to be matched with specific SAGE catalog sources.

My analysis of the IRAC colors and magnitudes of UCHII regions was based on the work done by GC09. GC09 used two simple mid-infrared color-selection criteria for their initial list of massive YSO candidates. They then analyzed the SEDs of that initial sample and obtained their final list of YSO candidates (see Section 1.2.1). Seale et al. (2009) spectroscopically confirmed the nature of the more luminous YSOs, including the four YSOs with UCHII emission detected in this work. Figure 3.3 shows a color-magnitude plot of the 855 'definite' massive YSOs identified by GC09. The triangles and diamonds represent the YSOs with UCHII regions detected by this work and by Indebetouw et al. (2004), respectively. They tend to cluster in an upper wedge of the

diagram, predominantly consisting of more luminous YSOs at 8.0 μm.

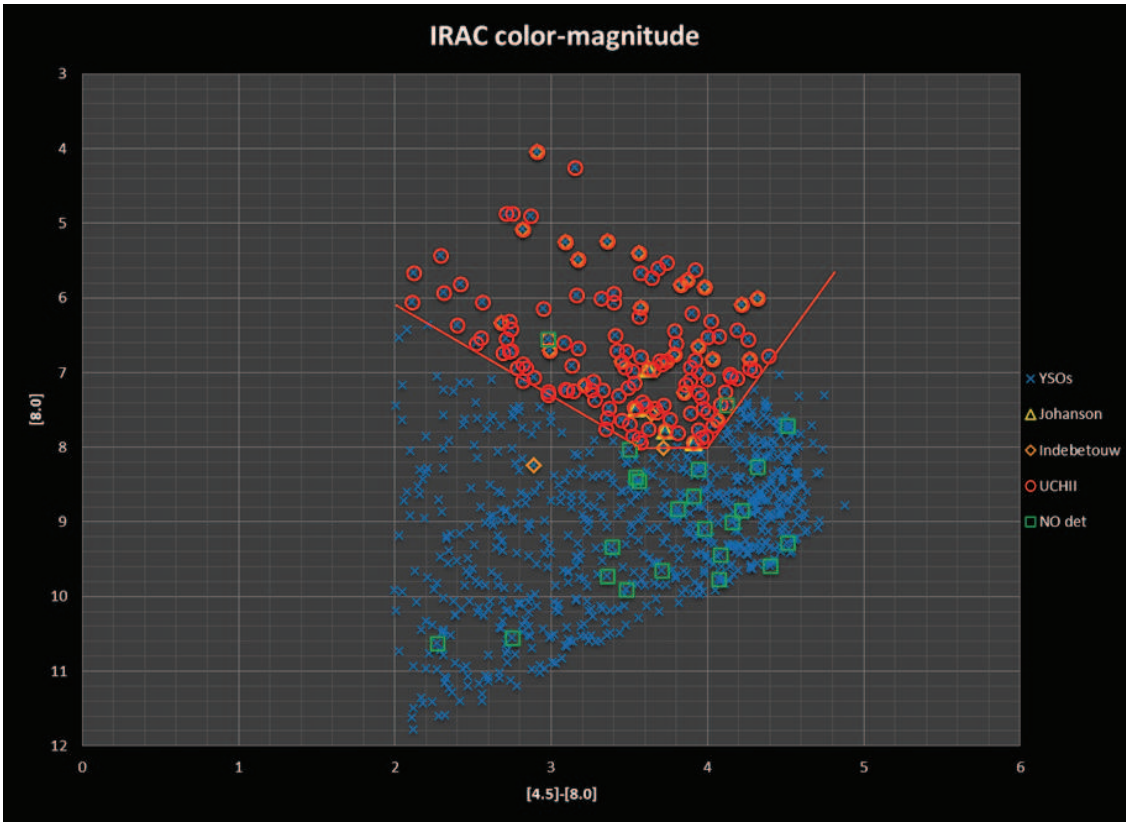

Figure 3.3 IRAC [4.5]-[8.0] vs. [8.0] color-magnitude diagram of GC09 YSOs. The blue crosses indicate GC09 massive YSOs, the yellow triangles indicate UCHII regions detected in this work, the orange diamonds indicate UCHII regions detected by Indebetouw et al. (2004), the red circles indicate the UCHII region candidates, and the green squares indicate massive YSOs with no observed UCHII region.

I empirically defined a region in the color-magnitude space containing the majority of detected UCHII regions. The selection cuts were made according to the criteria

$$\begin{aligned} [8.0] &< 8.0 \\ [8.0] &< 1.30([4.5]-[8.0])+3.47 \\ [8.0] &< -3.11([4.5]-[8.0])+20.5 \end{aligned} \tag{3.2}$$

where the brackets indicate the IRAC magnitude at the corresponding filter. I assert that most of the UCHII regions in the LMC (with a GC09 massive YSO association) lie within this color-

magnitude wedge. The first criterion was selected consistent with the assertment by GC09 that the most massive YSOs have $[8.0] < 8.0$. The second two were chosen to minimize the number of observed sources in the wedge with no detectable UCHII region. There will be (and are) some outlier UCHII regions, and there will be some massive YSOs in this wedge with no detectable UCHII region. This wedge of color-magnitude space correctly predicts $\sim$80% of UCHII regions detected in this work and in Indebetouw et al. (2004). Also note that this region of color-magnitude space contains all of the known UCHII regions associated with definite GC09 massive YSOs in the LMC save two. One of these sources fails only the first criterion because it has a $[8.0] = 8.01$. The other source lies in a portion of color-magnitude space that has been poorly sampled.

Ideally this sort of analysis would be done in the far-infrared with the *Spitzer* MIPS bands, because this is where most of the infrared radiation is emitted. The primary issue is the decreased resolution at the longer wavelengths compounds the source confusion problem. Otherwise I could have developed a color-color or color-magnitude criterion for the MIPS bands, extending the work established by Wood & Churchwell (1989b). This is something that could be done for galactic sources, where individual YSOs can be resolved. Figure 3.4 shows the positions of the UCHII region candidates overlayed on the MIPS 70 μm map of the LMC. Each candidate corresponds with bright far-infrared emission, consistent with the emission of UCHII regions peaking in the far-infrared (Churchwell 2002, p. 27).

Given the success rate of GC09 in correctly identifying massive YSOs (Seale et al. 2009), I estimate that $\geq$75% of the candidates will have a detectable UCHII region with the ATCA. Sources with no detectable UCHII region may be highly embedded and at a particularly early evolutionary stage. Thus with a more complete sample of the LMC UCHII regions, the fraction of candidates with UCHII regions will be directly related to the evolutionary timescales of massive YSOs. I recommend future targeted surveys for UCHII regions in the LMC should focus on this color-selected sample in the same way that previous searches were targeted toward IRAS sources. Completing the

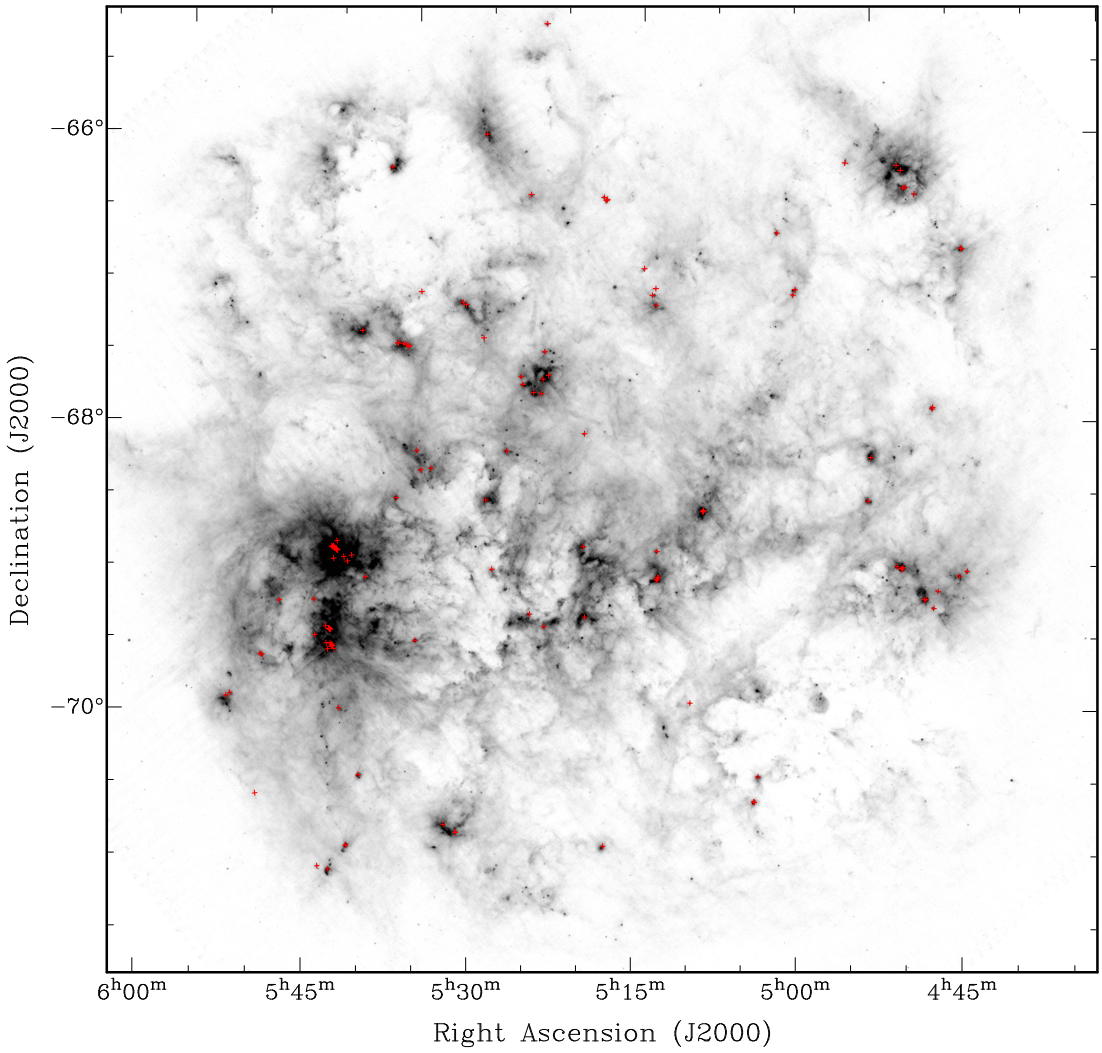

Figure 3.4 70 μm MIPS map tracing hot dust in the LMC. The red crosses mark the positions of the UCHII region candidates.

sample of UCHII regions in the LMC is one of the important steps in determining the current state of star formation in the LMC, and will lead to a greater understanding of massive star formation as a whole.

3.3 Miscellaneous Continuum Sources

An additional 23 radio sources were detected in my target fields. The positions, fluxes, and spectral indices of these sources are listed in Table 3.3. I searched the SAGE and SUMSS databases for associated emission with these objects, which are also listed in the table. Spectral indices are calculated from the available 6 GHz and 9 GHz data. Sources with steep negative spectral indices and associated infrared emission are more likely to be background AGNs.

Wide-field images of the detected continuum sources are shown in Figures 3.5, 3.6, and 3.7. There are some sources detected in the far-field of these images that are not displayed here.

Table 3.3 Other Continuum Sources at 6 and 9 GHz

Source	RA (J2000) h m s	Dec (J2000) ° ′ ″	$S_{6\ GHz}$[a] mJy	$S_{9\ GHz}$ mJy	α	Associations
N190-S1[b]	05 03 43.0	-70 49 14	3.03±0.27	···	···	SAGE, SUMSS
N190-S2	05 03 47.8	-70 40 35	0.43±0.06	0.67±0.25	1.1	SAGE
N190-S3[c]	05 04 09.4	-70 40 47	0.18±0.04	0.62±0.10	3.0	
N190-S5	05 04 31.4	-70 42 34	0.27±0.03	0.36±0.06	1.3	SAGE
N190-S6	05 04 41.2	-70 41 17	0.25±0.03	0.35±0.11	0.8	SAGE
N190-S7	05 04 54.2	-70 42 41	0.29±0.03	0.53±0.13	1.5	SAGE
N190-S8[b,d]	05 04 56.3	-70 45 11	6.79±0.38	10.9±0.63	1.2	SUMSS
N190-S9	05 05 02.2	-70 43 01	0.49±0.05	0.75±0.10	1.0	SAGE
N190-S10[e]	05 05 04.4	-70 44 52	0.35±0.05	0.51±0.10	0.9	SAGE
N190-S11[b,d]	05 05 09.1	-70 44 35	13.8±1.2	4.87±1.1	-2.5	SUMSS
N190-S12	05 05 27.7	-70 46 11	4.90±0.92	2.17±0.70	-2.0	SAGE, SUMSS
N191-S1	05 03 43.3	-70 55 49	0.70±0.08	···	···	
N191-S2	05 04 23.1	-71 01 50	2.79±0.33	···	···	
N191-S5	05 04 44.2	-70 49 58	1.78±0.11	1.71±0.20	-0.1	SAGE

Continued on next page...

Table 3.3 – Continued

Source	RA (J2000) h m s	Dec (J2000) ° ′ ″	$S_{6\ GHz}$[a] mJy	$S_{9\ GHz}$ mJy	α	Associations
N191-S6	05 05 03.2	-70 53 18	0.16±0.02	0.23±0.05	0.9	SAGE
N191-S7	05 05 12.4	-70 53 55	0.29±0.04	0.18±0.04	-1.2	SAGE
N191-S8	05 05 12.3	-70 57 22	0.63±0.05	0.47±0.09	-0.7	
N191-S9	05 05 17.4	-70 53 04	0.71±0.05	0.39±0.06	-1.5	SAGE
N191-S10[e]	05 05 17.9	-70 53 20	0.44±0.04	0.22±0.06	-1.7	SAGE, SUMSS
N191-S11	05 05 25.6	-70 56 12	4.39±0.22	2.64±0.17	-1.2	SAGE, SUMSS
N191-S12	05 05 28.1	-70 53 59	7.25±0.37	4.32±0.24	-1.3	SAGE, SUMSS
N206-S1	05 29 47.6	-71 06 37	0.77±0.05	0.54±0.04	-0.9	
N206-S2	05 30 09.1	-71 01 05	0.57±0.07	0.53±0.27	-0.2	SAGE
N206-S3	05 30 19.8	-71 06 40	0.17±0.03	0.10±0.03	-1.3	SAGE
N206-S6	05 30 31.3	-71 08 56	2.85±0.15	2.20±0.11	-0.6	SAGE, SUMSS
N206-S7	05 30 31.6	-70 57 40	6.01±0.94	···	···	SAGE, SUMSS
N206-S10	05 31 18.6	-71 03 18	0.25±0.05	0.22±0.07	-0.3	
N206-S11[b]	05 31 18.5	-71 05 17	···	1.77±0.37	···	
N206-S13	05 31 29.8	-71 07 22	0.53±0.06	0.53±0.07	0.0	SAGE
N206-S14	05 32 18.6	-71 07 45	1.73±0.12	2.08±0.44	0.5	SAGE, SUMSS

Note. — Missing numbers represent sources reported in Table 3.2.

[a] S_ν indicates the integrated flux density at frequency ν.

[b] Source is resolved with the ATCA synthesized beam.

[c] Indicates a potential high-frequency peaker such as seen in Rodríguez et al. (2014).

[d] Indicates a radio lobe.

[e] Indicates an AGN.

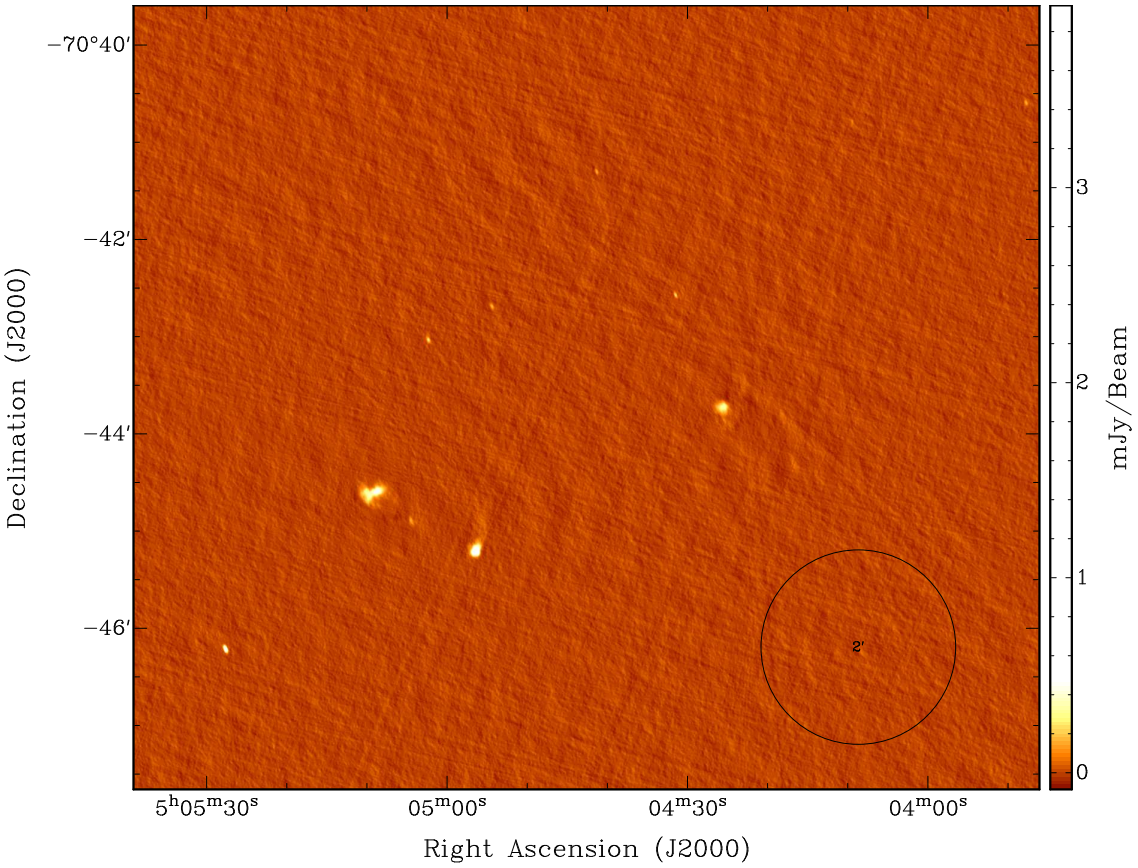

Figure 3.5 The 6 GHz radio continuum sources detected toward N190. A few of the far-field sources are not shown here. The circle at the bottom right has a diameter of 2′ and is shown for scale.

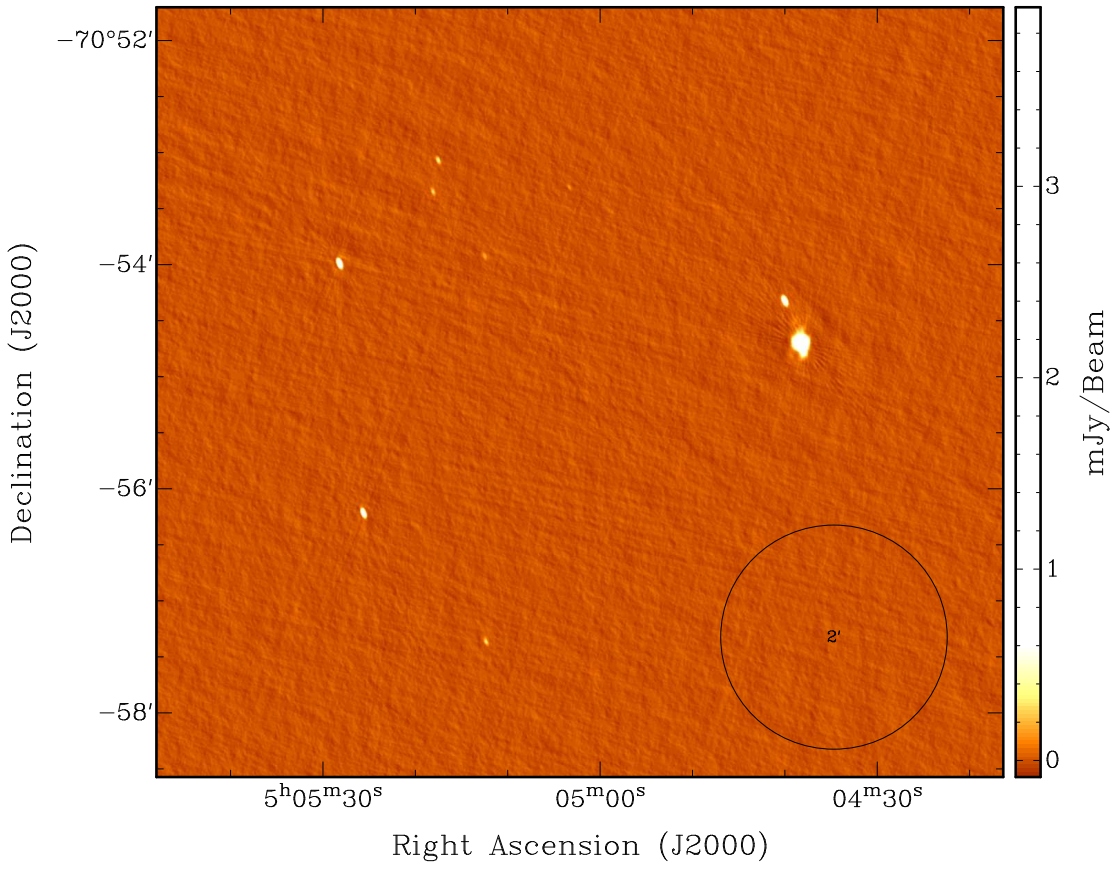

Figure 3.6 The 6 GHz radio continuum sources detected toward N191. A few of the far-field sources are not shown here. The circle at the bottom right has a diameter of 2′ and is shown for scale.

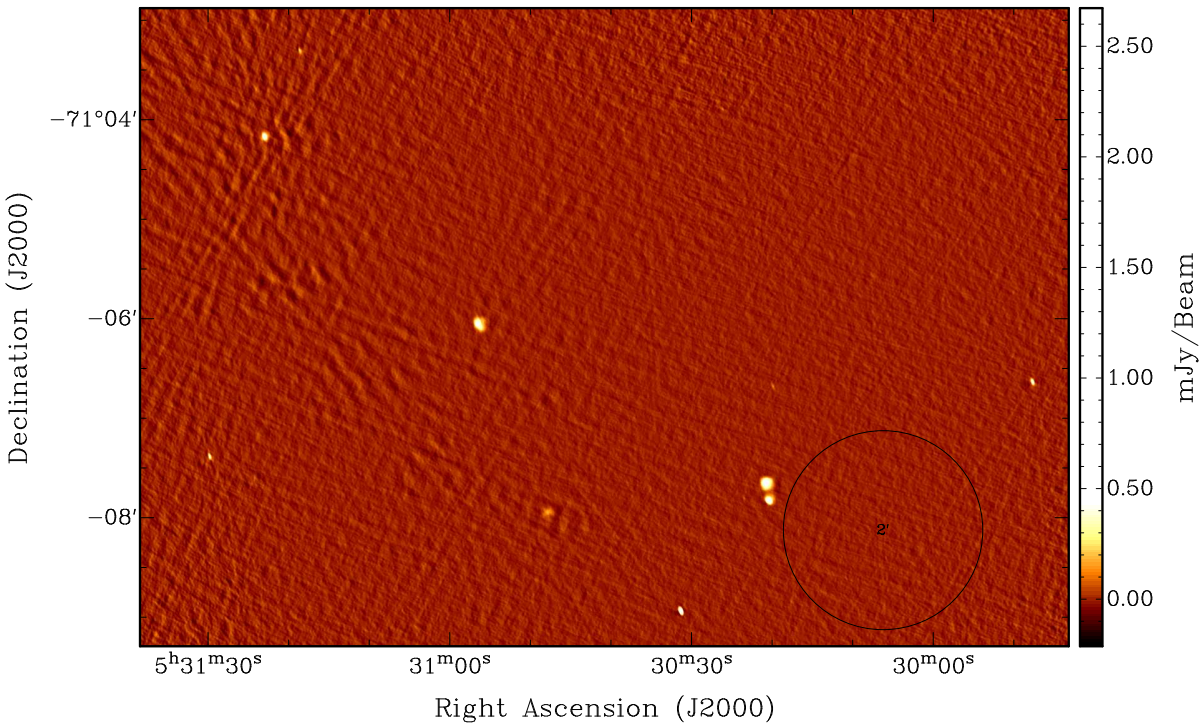

Figure 3.7 The 6 GHz radio continuum sources detected toward N206. A few of the far-field sources are not shown here. The circle at the bottom right has a diameter of 2′ and is shown for scale.

Chapter 4

Discussion and Analysis

4.1 N4A

N4A is the brightest region in the N4 H II complex. N4A is about 21.0″ in angular size (about 5.0 pc at the 50 kpc distance of the LMC) with two primary ionizing stars (Heydari-Malayeri & Lacavelier des Etangs 1994). Contursi et al. (2007) identified seven stars in the region in their near-infrared images, and suggested that their Star 2, Star 4, and Star 7 are YSOs (keeping with their nomenclature). They correspond to three definite YSOs identified by GC09. I detected three maser spots (N4A-M2, N4A-M3, N4A-M4) at different velocities toward Star 2. The locations of the detected masers relative to the IRAC 8.0 μm image are shown in Figure 4.1. The peak emission of N4A-M4 at 272.5 km s^{-1} corresponds to the peak CO emission of the "blue" molecular cloud as identified in Heydari-Malayeri & Lacavelier des Etangs (1994). However, it is the "red" component which they believe to be more directly linked with the N4A region. Although it peaks at 278.5 km s^{-1}, it would not be unusual for water masers to be spread by a mere 6 km s^{-1} from the systemic velocity (as is seen in Ellingsen et al. 2010).

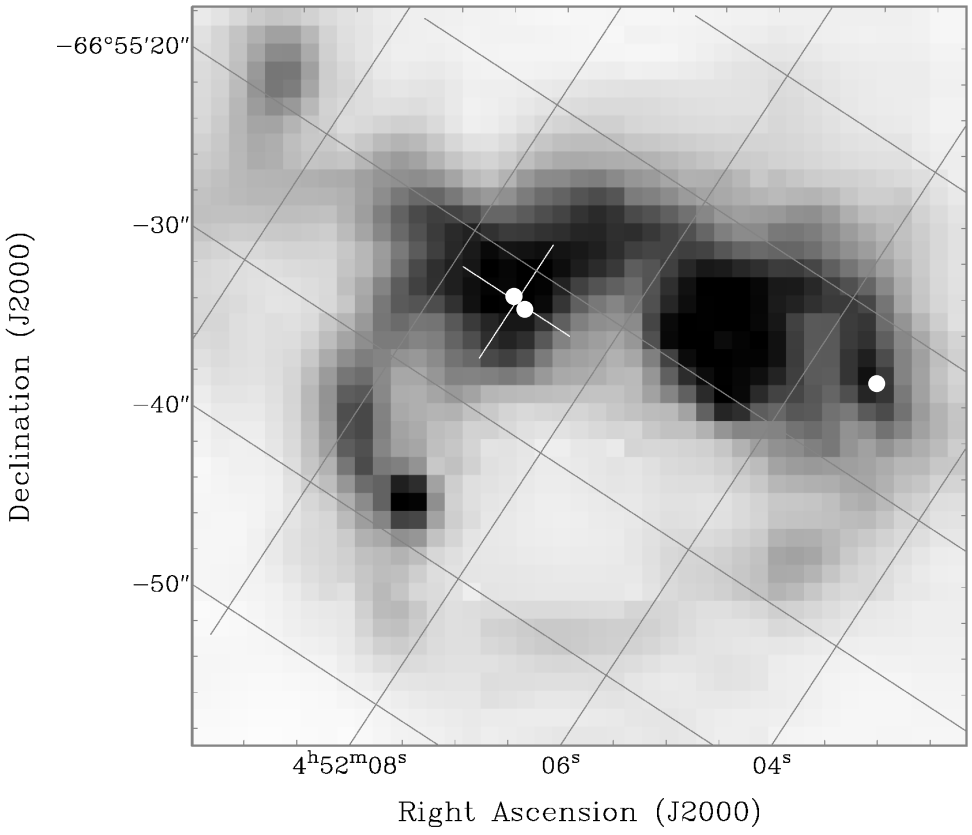

Figure 4.1 IRAC 8.0 μm image of N4A. The massive YSO identified by GC09 and Contursi et al. (2007) is indicated with a cross. The positions of masers detected in this work are shown as white dots. The filamentary structure with the associated maser N4A-M1 can be seen as an arc extending to the right of the brightest emission in the region. The gridlines are $10''$ apart, corresponding to a linear distance of $\sim$2.5 pc at the distance of the LMC.

Indebetouw et al. (2004) detected radio continuum emission at 4.8 GHz and 8.6 GHz toward Star 2. They suggested from the spectral index that the emission is attributed to thermal emission from an UCHII region caused by an O8V star. This classification is consistent with a massive central object, and I assert it is still embedded, based on the infrared analysis done by GC09 and Seale et al. (2009), as well as the presence of water masers, which normally indicate an early stage of formation (Ellingsen et al. 2010).

Water maser emission toward N4A had been recently discovered as reported by Imai et al. (2013). They used ATCA archival data from 2003, five years earlier than the data presented here. They likewise detected water masers toward the GC09 massive YSO over a similar velocity range. The spectral characteristics are very different, but high variability is very common for water masers (Felli et al. 2007). Given only the two observations and time between them, it is impossible to know all the details of their variability. I can only assume that the maser emission here has been somewhat persistent at least over a five year period (i.e. 2003-2008).

The maser spot N4A-M1 is not associated with a YSO candidate or any radio continuum emission detected by Indebetouw et al. (2004), nor was it detected in the archival data by Imai et al. (2013) (which may be simply due to variability). There is an infrared source within $0.9''$ detected in the SAGE data, but not at longer wavelengths, and there is also no associated 2MASS near-infrared point source. GC09 classified it as a diffuse source (J045205.39-665513.8) on the basis of it having no near- or far-infrared counterpart, and the fact that it is embedded in the aforementioned dust filament. The filamentary structure was identified by Heydari-Malayeri & Lacavelier des Etangs (1994). Even the spectral analysis by Seale et al. (2009) initially classified it as a highly-embedded YSO, but they argued in favor of the GC09 interpretation, noting that such diffuse objects are "spectroscopically indistinguishable from YSOs" in that limited spectral range.

Given the corresponding infrared evidence, a detection of a water maser is strong evidence that this source is indeed a YSO. It is interesting to note that GC09 state that their diffuse sources may harbor low- or intermediate-mass YSOs. It is not uncommon for low-mass YSOs to exhibit water maser emission (Wilking et al. 1994, for example), but it would be the first detection of an extragalactic maser associated with a low-mass YSO (Imai et al. 2013). However, GC09 and Seale et al. (2009) both use the criterion that to first order, YSOs with an IRAC 8.0 μm magnitude less than eight ($[8.0] < 8.0$) indicates they are high-mass. For J045205.39-665513.8, $[8.0] = 7.74$. In addition, Ellingsen et al. (2010) found that water maser emission in the LMC occurs prefer-

entially toward the more luminous and redder GC09 definite YSOs. They identified criteria in color-magnitude space which identify regions where maser sources are most likely to be found, and the J045205.39-665513.8 colors satisfy these criteria. Although more study will be needed to determine its mass, I assert it is a YSO.

4.2 N190

The emission nebula N190 is a poorly studied, inconspicuous H II region near the NGC 1833 star cluster. Both the SUMSS and Dickel et al. (2005) radio surveys detected a compact H II region on order of $2'$ across. The peak emission of this compact H II coincides with the brightest mid-infrared source in the region, identified by GC09 as a massive YSO and spectroscopically confirmed by Seale et al. (2009). Because I maximized my observations for small scale sensitivity (insensitive to extended structure greater than $30''$), this more extended region went virtually undetected. I did detect an even more compact H II region (N190-HII1), offset from the peak of the extended emission by about $10''$, and separated from the YSO by about $5''$. This represents the first detection of this smaller structure at radio frequencies. This source spatially and morphologically coincides with an optical H II region as seen in the MCELS Hα image in Figure 4.2.

I report the presence of two water masers, N190-M1 associated with the GC09 massive YSO, and N190-M2 closer to N190-HII1. These masers are new detections, and are reported for the first time in the literature in Johanson et al. (2014). These masers will be useful in maser proper motion studies of the LMC to determine galactic rotation, such as the one proposed by Imai et al. (2013). They probe a region of the LMC devoid of any known masers, and therefore provide a useful constraint on the galactic dynamics in that region.

Figure 4.3 shows the IRAC 4.5 μm contours of the region with maser positions indicated. The 2MASS data show independent point sources here, each separated from the masers by less than

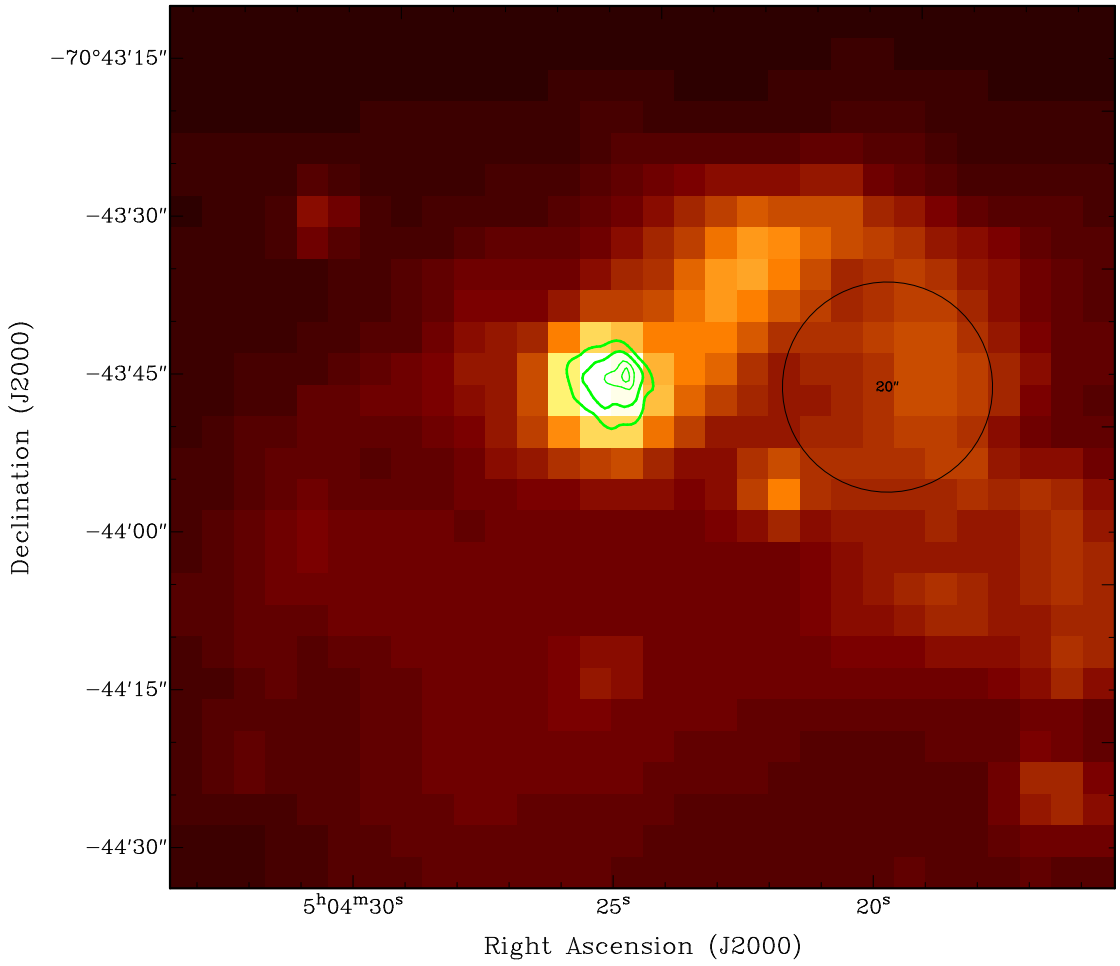

Figure 4.2 MCELS Hα image of N190 with the 6 GHz radio contours (0.1, 0.2, 0.3, and 0.34 mJy beam^{-1}) of N190-HII1 overlayed. The alignment between the two is clear. The circle is 20$''$ in diameter, corresponding to a linear distance of $\sim$5 pc at the distance of the LMC.

2$''$. The source associated with the compact H II region shows a faint counterpart in the 4.5 μm data, but not in the other IRAC bands. This is reminiscent of extended green objects (EGOs) seen in the Milky Way, extended regions of emission often indicating shocked gas from massive YSO outflows (Cyganowski et al. 2013). Finding water masers toward these EGOs has been met with great success, where Cyganowski et al. (2013) detected water masers toward 68% of these structures.

I propose that the compact H II region N190-HII1 is a more evolved star-forming region with most of the UV flux being provided by a Zero Age Main Sequence star of spectral type B0V based on the radio intensity. I also propose that it is accompanied by other young massive stars still forming, as evidenced by the presence of a nearby water maser. I also affirm the presence of the GC09 high-mass YSO, consistent with the spectroscopy by Seale et al. (2009), the presence of a water maser, and the more extended H II region imaged in the SUMSS and Dickel et al. (2005) surveys.

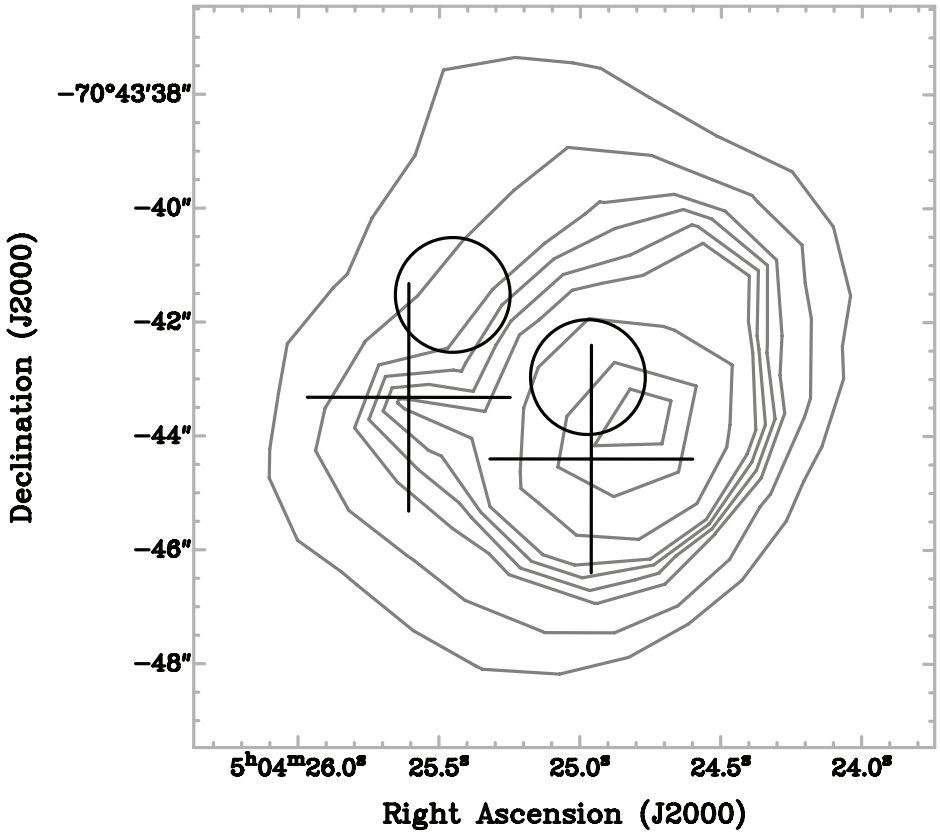

Figure 4.3 IRAC 4.5 μm contours of N190. Crosses indicate the positions and uncertainties of 2MASS J05042500-7043444 and 2MASS J05042559-7043434. The circles indicate the positions and uncertainties of the newly detected masers. The contours (10, 15, 21, 24, 27, 30, 40, 60, and 80% of the peak intensity at 13 MJy sr^{-1}) have a peak at the GC09 massive YSO, but they do show some emission associated with 2MASS J05042559-7043434 near N190-M2.

4.3 N191

Both the SUMSS and Dickel et al. (2005) surveys detected a single, bright radio point source in N191. GC09 identified three massive YSO candidates in the region, two of which were confirmed by the observations of Seale et al. (2009) (the third wasn't bright enough to be selected for their observations). N191 has been studied in detail by Selier & Heydari-Malayeri (2012). They obtained photometry on the stellar content of the region including the three GC09 YSOs. It is interesting to note that Seale et al. (2009) identifies a massive YSO at the position of the primary ionizing star, whereas GC09 and Selier & Heydari-Malayeri (2012) do not. One potential resolution is source confusion, likely because the whole compact H II region contains several ionizing stars and potentially several YSOs given its 2.4 pc diameter (Selier & Heydari-Malayeri 2012).

I resolved the single SUMSS and Dickel et al. (2005) source into two compact H II regions (see Figure 4.4). The brighter compact H II region (N191-HII1) is associated with the primary ionizing star in the region as identified by Selier & Heydari-Malayeri (2012). The morphology of N191-HII1 matches the optical and infrared morphology, as seen in Figures 4.4 and 4.5. Selier & Heydari-Malayeri (2012) identify the primary ionizing source as an O5V star based on the ionizing photon flux determined from Hβ emission from the whole H II region. However, from the spectrum of the star they classify it as an O8.5V star. Selier & Heydari-Malayeri (2012) attribute the discrepancy to potentially hidden hot stars that lie along the upper end of the color-magnitude diagram. The Seale et al. (2009) massive YSO could potentially be one of these "hidden" stars. My classification based on the radio continuum emission places it as an O8V star, favoring the spectral classification.

The dimmer N191-HII2 is a point-source, and represents the first detection in the radio. Given its association with the massive YSO GC09 J050439.85-705419.0 and the Selier & Heydari-Malayeri (2012) object N191-YSO1, I classify this as an UCHII region. Based on the radio emission, the Crowther (2005) system classifies this object as a B0V star. I also looked at the

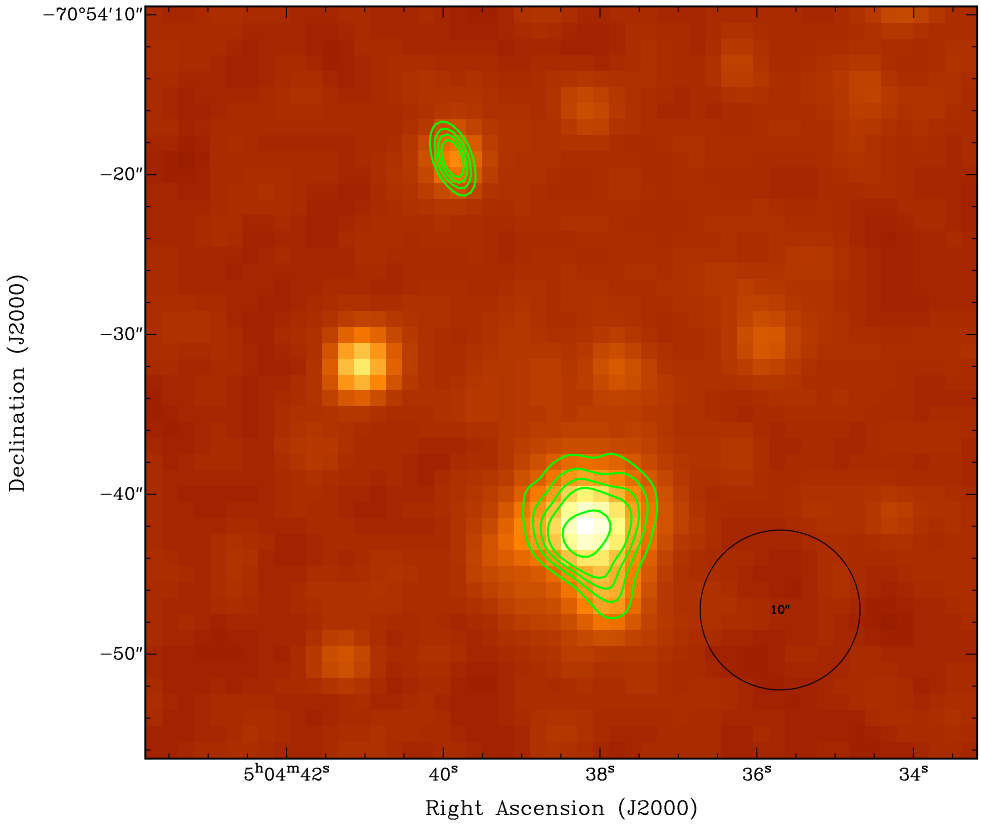

Figure 4.4 2MASS J band image overlayed with 6 GHz contours (0.7, 1.2, 1.7, 2.2 and 3.3 mJy beam^{-1}) toward N190-HII1 and N190-HII2. The circle is 10″ in diameter, corresponding to a linear distance of ∼2.5 pc at the distance of the LMC.

best Robitaille et al. (2007) model that fits the known infrared data. The best-fit SED is shown in Figure 4.6. Based on the total luminosity of the star given the YSO model, the corresponding Crowther (2005) spectral type is an O9.5V, which agrees remarkably well with the radio.

It is also interesting to note that the other YSO had no detectable UCHII region. This source was even predicted to have an UCHII region based on its position in the $[4.5]-[8.0]$ vs. $[8.0]$ color-magnitude diagram. This could indicate that the source is in its earliest stages of evolution, before the onset of the UCHII phase. The fraction of sources like this in the entire UCHII region sample could yield insight into the evolutionary timescales of massive YSOs, namely the fraction of their life as a YSO that they spend without a detectable UCHII region.

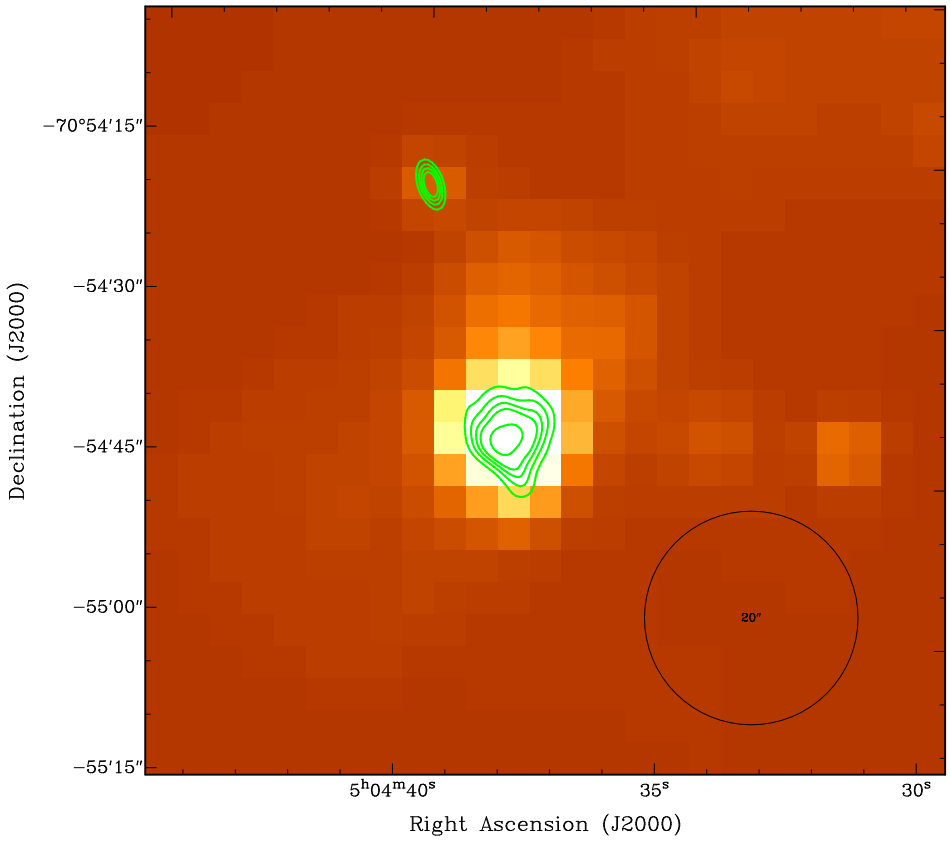

Figure 4.5 MCELS Hα image with the same contours in Figure 4.4. The circle is 20″ in diameter, corresponding to a linear distance of ∼5 pc at the distance of the LMC.

4.4 N206

N206 is an extended H II region which contains a ridge compressed by past supernovae and massive stellar winds (Dunne et al. 2001; Kavanagh et al. 2012). This compressed medium has instigated a flurry of energetic massive star formation (Gorjian et al. 2004). The previous radio emission detected here is mostly the diffuse, extended emission associated with the region as a whole. Indebetouw et al. (2004) report five compact sources toward N206. I was able to confirm their detections, but provided much more accurate fluxes. I note that their sources B0531-7106(SE) and B0531-7106(SW3) don't appear to be compact H II regions associated with star formation and that B0521-7106(SW2) is actually two UCHII regions (N206-HII1 and N206-HII2) associated with

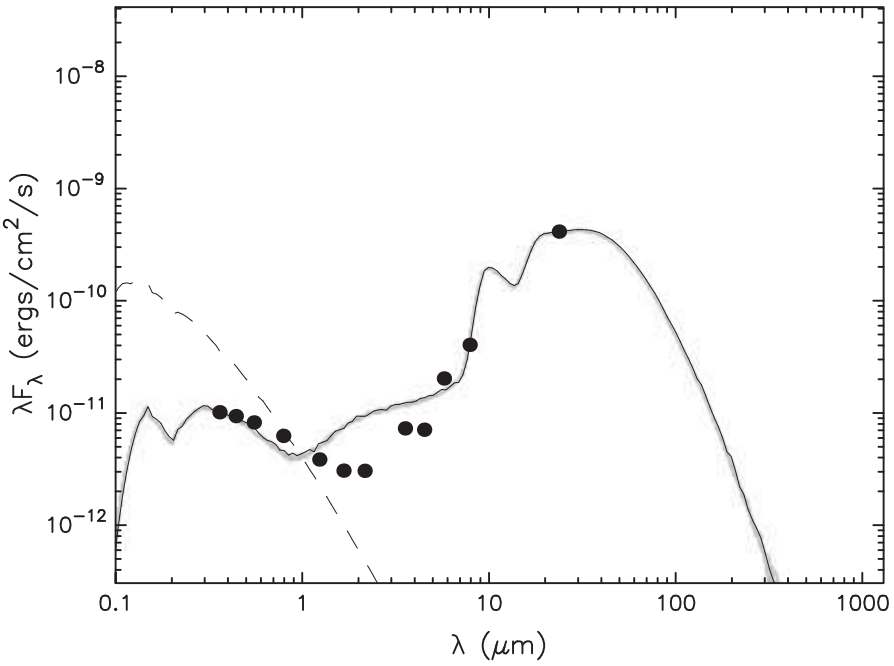

Figure 4.6 The best-fit SED model of Robitaille et al. (2007) for N191-HII2. Fit was based on flux measurements in the UBVI filters from Zaritsky et al. (2004), the 2MASS JHK bands, the four IRAC bands and the 24 μm MIPS band. Other possible fits are shown in light gray.

two different GC09 massive YSOs, both of which are confirmed by Seale et al. (2009). I have also detected an additional compact H II region not detected by Indebetouw et al. (2004) (N206-HII3). In total, there are five compact H II regions, three of which are classified as UCHII given their association with GC09 high-mass YSOs. Figure 4.7 shows the positions of the compact H II regions in relation to the mid-infrared emission from the region.

The two UCHII regions N206-HII1 and N206-HII2 are shown in Figure 4.8. Actually all four of the infrared sources are GC09 massive YSOs, but the two to the east exhibit no UCHII emission

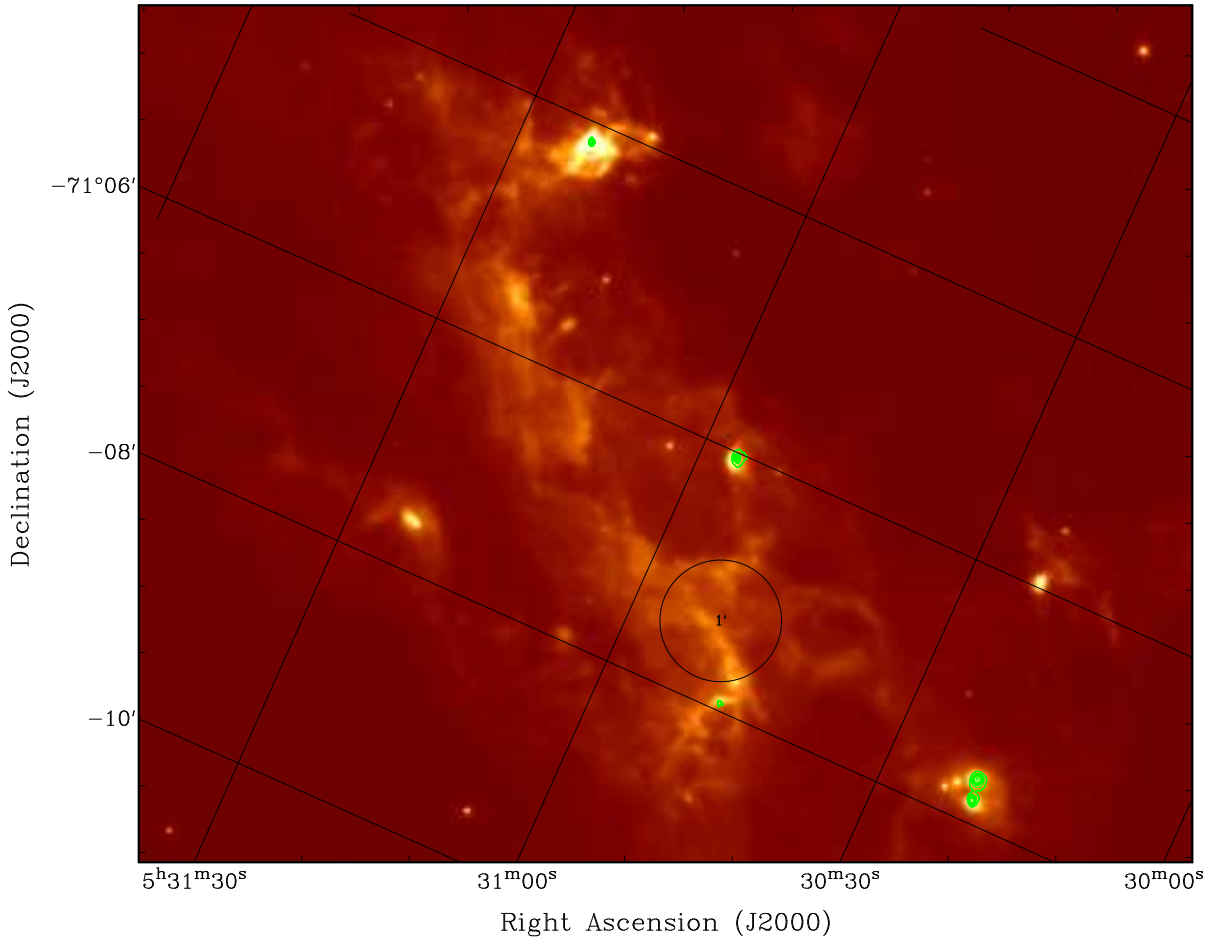

Figure 4.7 IRAC 8.0 μm image of N206 with 6 GHz contours (0.17, 0.2, 0.4, 0.5, 0.6, 0.7, 0.8, 0.9, and 1.0 mJy beam^{-1}) marking the five compact H II regions. The circle is $1'$ in diameter, corresponding to a linear distance of $\sim$15 pc at the distance of the LMC.

either because they have not reached that stage in their evolution yet or they are not massive enough to produce detectable emission. Model SEDs were fitted for both N206-HII1 and N206-HII2 and are plotted in Figure 4.9. Based on the total luminosity from the best-fit model, the corresponding Crowther (2005) spectral type for N206-HII1 is a B1.5V and for N206-HII2 is a B1V. Both spectral types determined by the radio emission predict an earlier spectral type than what is predicted by the infrared models. This again suggests a later evolutionary stage for both of these sources, where

the dust has been dissipated somewhat. Since both sources are slightly extended, this is consistent with more evolved UCHII regions. Neither source is visible in the optical and they are therefore still embedded in their natal molecular cloud.

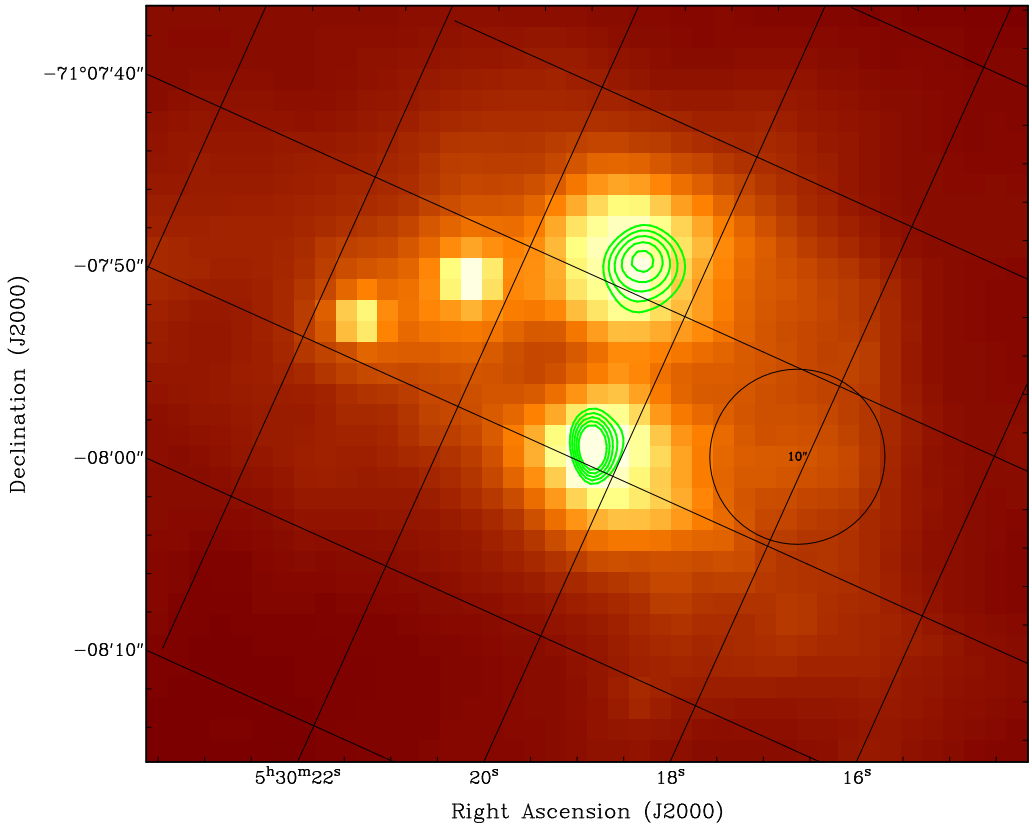

Figure 4.8 IRAC 8.0 μm image overlayed with 6 GHz contours (0.6, 0.7, 0.8, 0.9, and 1.0 mJy beam^{-1}) toward N206-HII1 and N206-HII2. The circle is 10″ in diameter, corresponding to a linear distance of ∼2.5 pc at the distance of the LMC.

Figure 4.10 shows a 2MASS infrared image with the 6 GHz radio contours of N206-HII3 overlayed in the upper panel and a *Spitzer* image showing the dust structure in the lower. The bright source is a luminous main-sequence O7.5V star (Bonanos et al. 2009). The fainter source is associated with N206-HII3. The O7.5V star appears to be at the center of an intestellar bubble, while N206-HII3 lies at the edge. The bubble is presumably hollowed out by the stellar winds of the massive star. If so, then I assert that this is an example of induced star formation from the

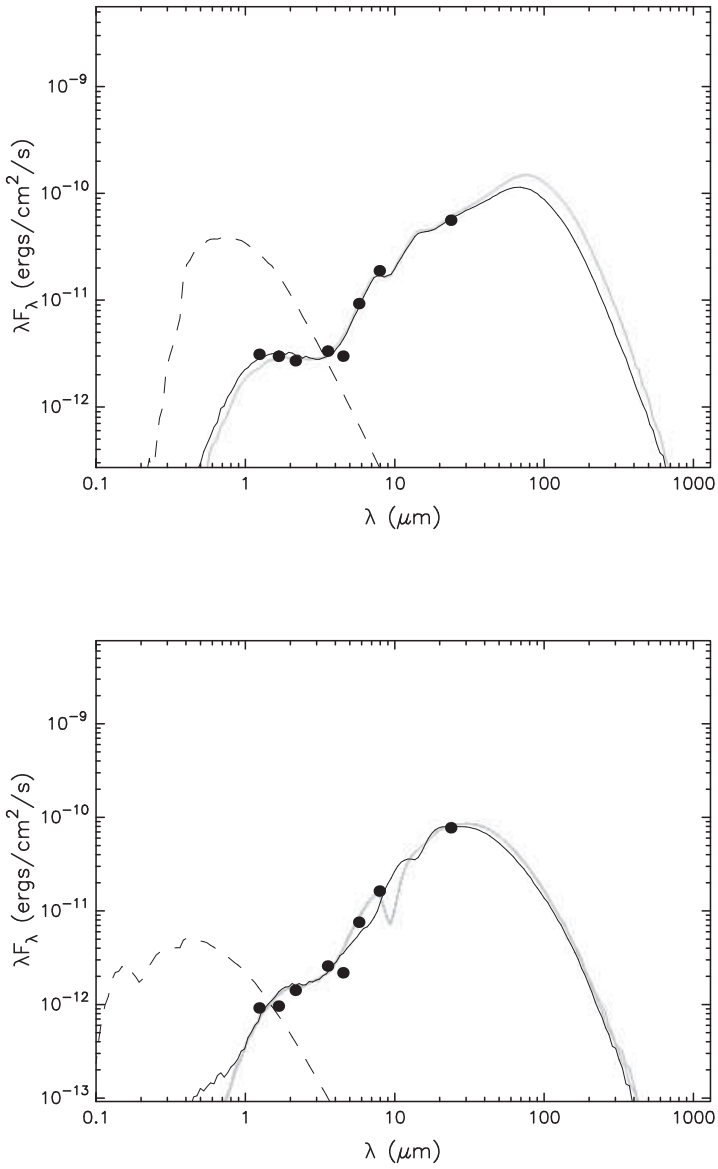

Figure 4.9 The best-fit SED models of Robitaille et al. (2007) for N206-HII1 (top) and N206-HII2 (bottom). Fit was based on flux measurements in the 2MASS JHK bands, the four IRAC bands and the 24 μm MIPS band. Other possible models are shown in light gray.

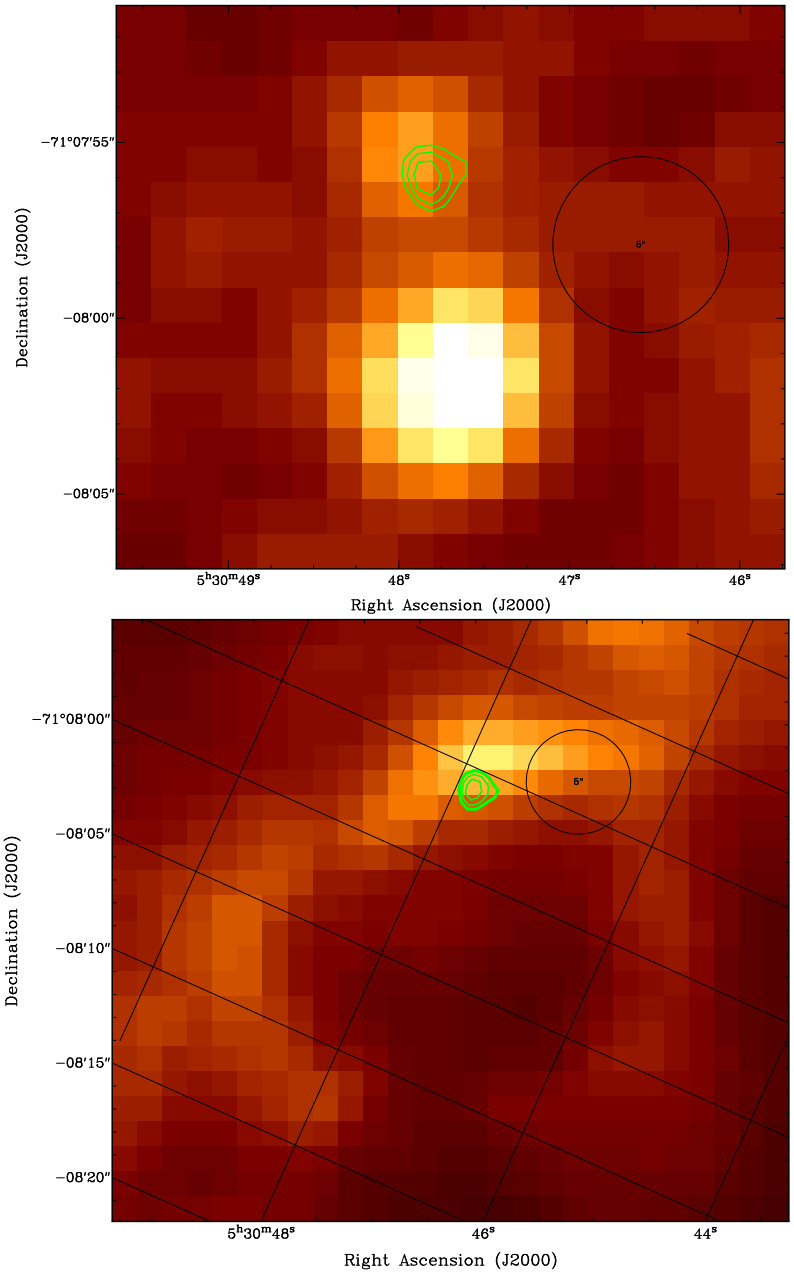

Figure 4.10 *Top*: 2MASS J band image showing the bright O7.5V star in the center, overlayed with 6 GHz contours (0.25, 0.26, and 0.27 mJy beam^{-1}) toward N206-HII3. The circle is 5″ in diameter, corresponding to a linear distance of ∼1.2 pc at the distance of the LMC. *Bottom*: IRAC 8.0 μm image showing an infrared shell condensed by winds from the O7.5V star. Overlayed with the same contours and circle as above.

stellar winds of a massive star.

Figure 4.11 compares the radio and infrared emission for N206-HII4. The radio and infrared morphology match well, with the denser part of the emission on the left of the source and on the right the emission is less dense. This morphology matches that of a blister region, where the ionizing star has broken through one part of its natal cloud, allowing the photons to flow freely on that side. This morphology is similar to that of M42 in Orion. Based on the radio emission, I classify the ionizing star as an O9.5V that is producing a rapidly growing H II region.

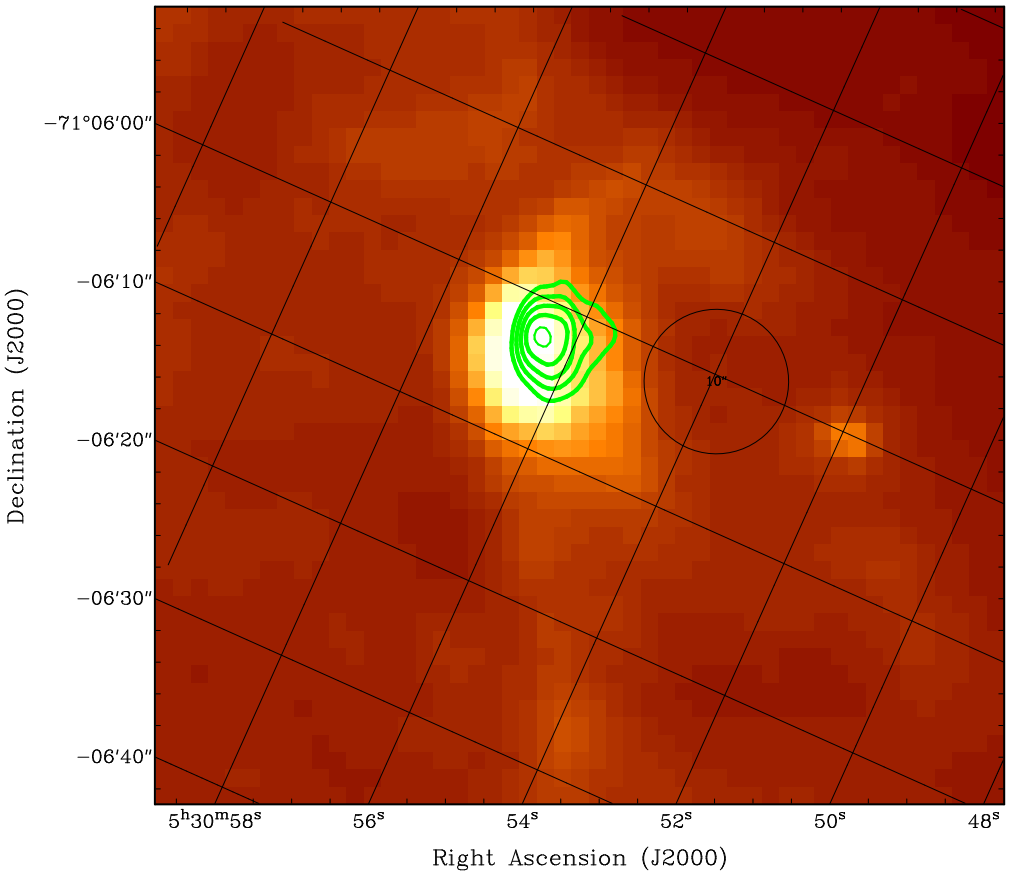

Figure 4.11 IRAC 8.0 μm image overlayed with 6 GHz contours (0.2, 0.3, 0.4, 0.5, and 0.6 mJy beam^{-1}) toward N206-HII4. The circle is 10″ in diameter, corresponding to a linear distance of ∼2.5 pc at the distance of the LMC.

N206-HII5 is associated with a bright infrared knot identified by Gorjian et al. (2004) and is

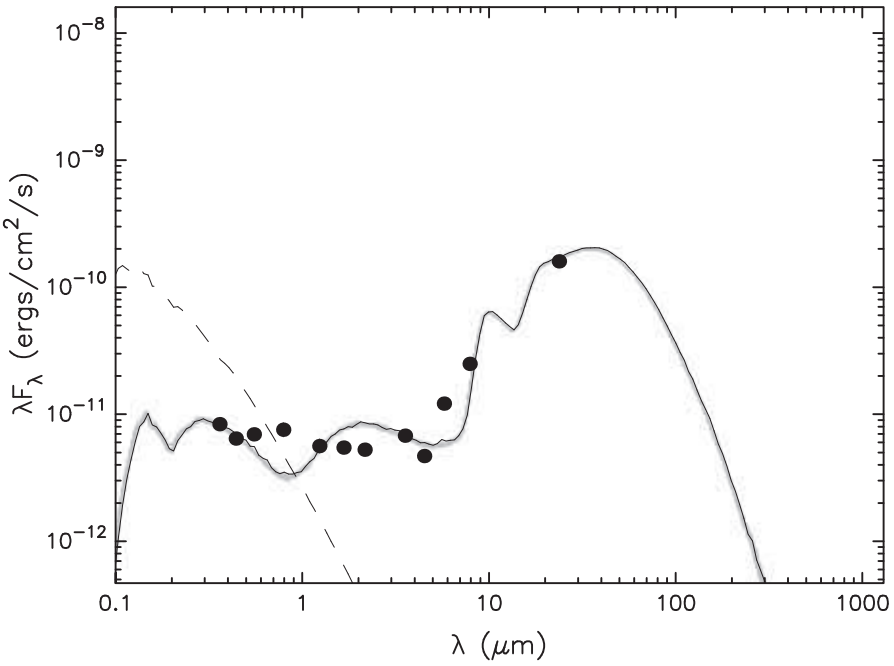

Figure 4.12 The best-fit SED model of Robitaille et al. (2007) for N206-HII5. Fit was based on flux measurements in the UBVI filters from Zaritsky et al. (2004), the 2MASS JHK bands, the four IRAC bands and the 24 μm MIPS band. Other possible fits are shown in light gray.

probably the primary ionizing source for this region. I classify this object as an UCHII region based on the compact radio emission associated with the bright infrared source that has been classified as a massive YSO by GC09. The best-fit SED model from Robitaille et al. (2007) is shown in Figure 4.12. The infrared spectral type based on the total luminosity of the star given the YSO model is a B0.5V, again in good agreement with the B0V spectral type determined by the radio emission. This UCHII region was detected amidst some larger, diffuse radio emission as can be seen in Figure 4.13. I do note the presence of a *Chandra* x-ray source, and suggest that the area

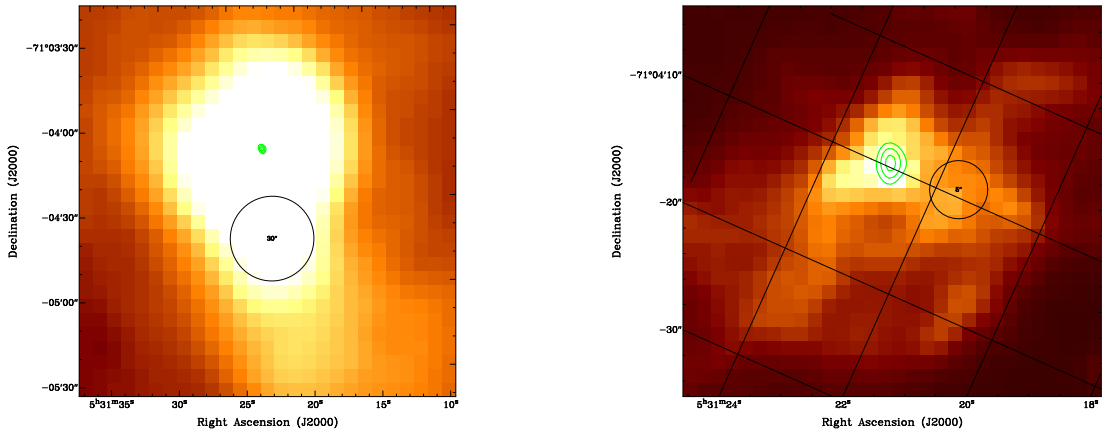

Figure 4.13 *Left*: Dickel et al. (2005) 8.6 GHz image overlayed with 6 GHz contours (0.6, 0.8, and 1.0 mJy beam^{-1}) toward N206-HII5. The circle is 30″ in diameter, corresponding to a linear distance of ∼7.3 pc at the distance of the LMC. *Right*: IRAC 8.0 μm image overlayed with the same contours as in the top panel. The circle is 5″ in diameter, corresponding to a linear distance of ∼1.2 pc at the distance of the LMC. The association with the GC09 YSO is clear, illustrating the importance of the high-resolution observations used in this work.

probably suffers from source confusion, where there are probably many stars. However, I assert that N206-HII5 is the GC09 massive YSO, responsible for the bright infrared emission.

4.5 Active Galactic Nuclei

There are several other continuum sources in the field of view which are not associated with the star-forming regions or GC09 YSOs. These sources could include supernova remnants, planetary nebulae, or background radio galaxies. Sources with associated infrared emission and large negative spectral indices are likely AGNs. Several of these sources are detected for the first time in these observations.

The contours in Figure 4.14 show several point sources detected toward N191 at 6 GHz. Some of these sources have SUMSS radio and SAGE infrared counterparts. Their infrared colors need to be analyzed to determine their nature. Most notable is the northernmost source N191-S10 near

the top of the image. Kozłowski & Kochanek (2009) had classified this source as an AGN based on its IRAC colors. The radio emission here confirms that this source is an AGN. It is possible that some of the other sources are AGNs as well, but their emission is not detected at enough IRAC bands to determine colors.

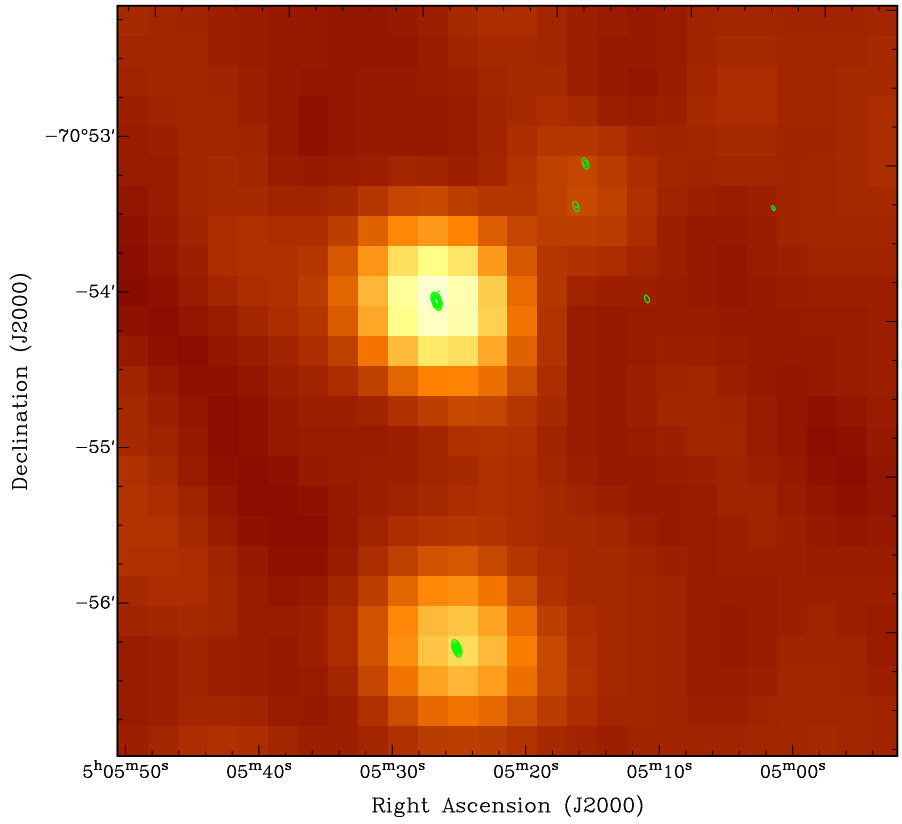

Figure 4.14 SUMSS 843 MHz image overlayed with 6 GHz contours (0.1, 0.3, 0.8, 1.0 and 2.0 mJy beam^{-1}) in the vicinity of N191.

Although many of these sources require more observations and more information to classify, three are easily identified by their collective morphology (N190-S8, N190-S10, and N190-S11). Figure 4.15 shows the observed 6 GHz radio contours on the SUMSS image. The low-resolution SUMSS image shows two bright point-sources, which are easily resolved in my data. I also detected a previously unknown source between the two. Figure 4.16 shows a *Spitzer* MIPS 24 μm image, where there is a definite infrared counterpart with the central radio source. The fact that the

radio source peaks in the far-infrared is consistent with the SED of an AGN (Sanders 1999). The whole system is a case of a classic, double-radio lobed galaxy, consistent with the classification by Flesch & Hardcastle (2004), except now the proper host galaxy has been correctly identified.

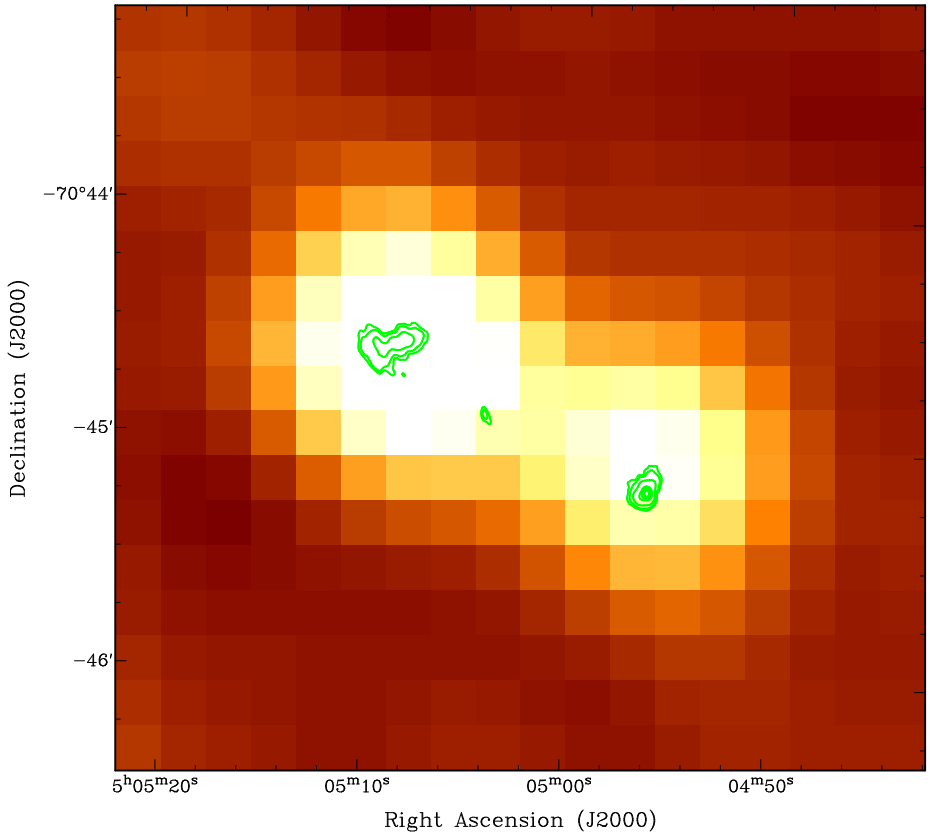

Figure 4.15 SUMSS image of a double-lobed radio galaxy. The 6 GHz contour overlay (0.08, 0.13, 0.30, 0.8, 1.0 and 1.2 mJy beam^{-1}) resolve the lobes and reveal the central galaxy.

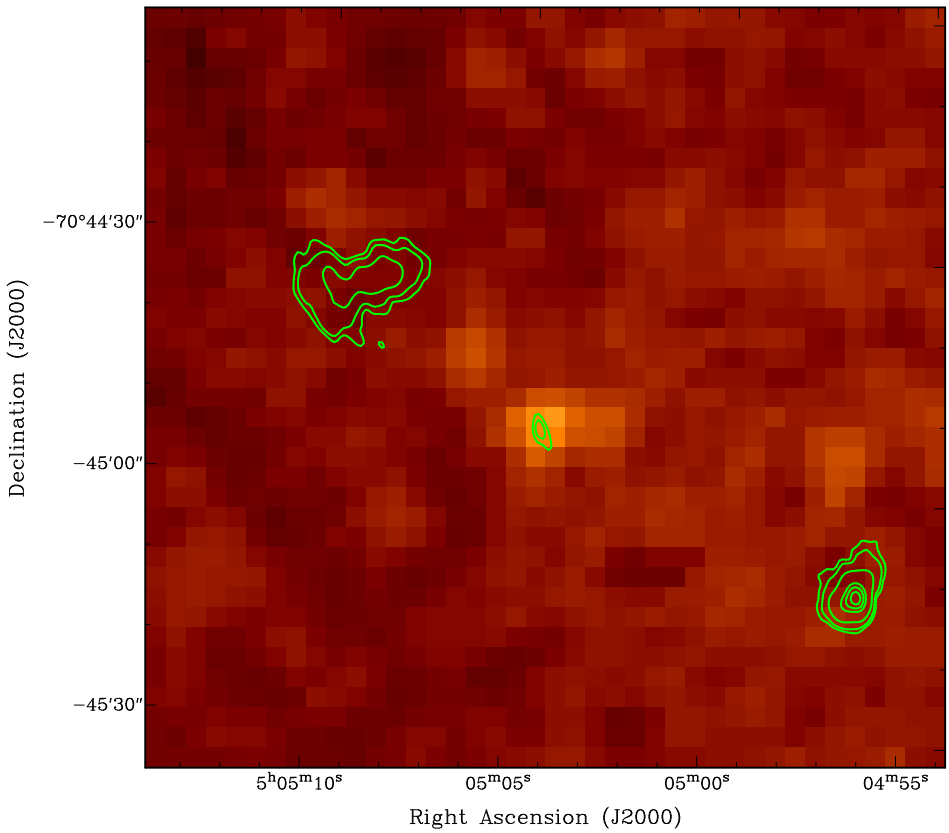

Figure 4.16 MIPS 24 μm image showing the infrared counterpart to the radio galaxy. The radio contours are the same as in Figure 4.15.

Chapter 5

Conclusions

I have presented a survey of radio emission toward four massive star-forming regions in the LMC, N4A, N190, N191, and N206. The key results of the observations are enumerated as follows:

1. A total of 42 radio detections were made including 27 new radio sources not seen in previous radio surveys. Many of these sources are likely AGNs, but more observations are needed to classify them. I was able to identify two new AGNs, confirming one candidate based on its IRAC colors and discovering the host of a classic, double-lobed radio galaxy for the other.

2. I searched for maser emission from water vapor toward N4A, N190, and N206. I detected four 22.2 GHz water masers toward N4A and N190. Three of these are new detections, increasing the total number of water masers around young stars in the LMC to 23 in 15 regions. Two of the masers (containing maser spots N4A-M2, N4A-M3, N4A-M4, and N190-M1), were associated with GC09 massive YSOs, providing strong support for their classification. This supports the conclusions of Ellingsen et al. (2010), namely that massive YSOs with associated water maser emission are more luminous and have redder colors, indicating highly embedded objects. The other two masers (N4A-M1 and N190-M2) identified new massive YSOs. The N4A-M1 maser did match the initial criterion for a YSO in both the GC09 and

Seale et al. (2009) surveys. The N190-M2 maser is not very bright in the IRAC bands, and therefore was not included in the GC09 survey. All in all, the methods used by GC09 appear to be successful in identifying massive YSOs.

3. I also searched for 6.7 GHz methanol and 6.035 GHz excited OH maser emission toward N190, N191, and N206. No detections were made for either species. The lack of 6.7 GHz masers (which exclusively trace massive YSOs) agrees with the results of the survey by Green et al. (2008), even though I observed known massive YSOs at an order of magnitude higher sensitivity. This supports the hypothesis in Green et al. (2008) that there may be a lack of these molecules due to an underabundance of methanol in the LMC.

4. A total of eight compact H II regions were detected, four of which I classified as UCHII regions. The other four appear to be more evolved compact H II regions with strong optical and near-infrared components. Four of these are new detections. The other sources represent a substantial improvement on fluxes over previously published values. Using simple symmetry and standard H II region physics, I determined the equivalent single-ionizing-star spectral type needed to provide the observed ionizing flux. I also used the infrared SED models of Robitaille et al. (2007) to model the physical characteristics of the massive YSOs with UCHII emission. I then compared the spectral type determined by the modeled luminosity with the spectral type based on the radio intensity. This analysis suggests that this may be a good method to determine the relative amount of dust around the massive YSO, and thus get a measure of the evolutionary state of the star.

5. I examined the placement of the UCHII regions detected in this work and those detected by Indebetouw et al. (2004) in an IRAC $[4.5]-[8.0]$ vs. $[8.0]$ color-magnitude diagram. I defined a region in color-magnitude space that incorporated the majority of the known UCHII regions. This yielded a list of 136 UCHII region candidates across the LMC, $\geq$75% of which

are expected to be confirmed. I suggest that future searches for UCHII regions be based off these IRAC colors, as opposed to previous criteria used in the Milky Way. Identifying all of the massive YSOs and UCHII regions in the LMC would provide a framework for high-resolution studies of these objects in order to piece together star formation history of an entire galaxy. Aspects affecting star formation, such as the mass of the star, evolutionary state, its position within the LMC, the metallicity of their parent clouds, and the abundance of masers could all be studied and compared to the Milky Way, leading to an increased understanding of massive star formation and star formation on a galactic scale.

There are still questions about star formation left unanswered, such as

- *What are the physical processes through which massive stars form? Is there one dominant mechanism or several? What are the observable signatures of each?*
- *Why is there an underabundance of methanol masers in the LMC? Is there an underabundance of molecules in general because of a strong ambient UV field, or is it related to the mechanics of star formation in the LMC vs. the Milky Way?*

The available instrumentation and surveys can address these important questions. Future observations with the ATCA would involve observing these same star-forming regions for ground-state OH emission, which is particularly associated with UCHII regions. This would provide a complete survey of the major maser species associated with massive star formation toward these regions. Follow-up observations are also necessary on the UCHII region candidates to verify their nature. If it were the case that OH masers in the LMC are as common toward UCHII regions in the LMC as in the Milky Way, this could provide a dramatic increase in the number of known masers in the LMC. The massive YSOs with associated radio emission provide excellent targets for high-resolution observations using the Atacama Large Millimeter/submillimeter Array (ALMA), which could resolve individual YSOs even at the distance of the LMC. The plethora of molecular lines

observable with ALMA would provide an additional test to the abundances of molecular species in the LMC. For example, ALMA observations of the (3,2) hyperfine transition of NH_3 can trace molecular gas around massive YSOs at a resolution one hundred times higher than what is possible with the ATCA. Observations of CS could pinpoint potential groups of massive YSOs in regions where I have assumed a single, dominant source. Abundances of both of these molecules could also provide an additional measure of molecular abundances in LMC star-forming regions.

Given its proximity and active star-forming regions, the LMC is an excellent specimen for the study of massive star formation. With just a few observations and the available corresponding infrared data from SAGE, I have been able to determine the large-scale distribution of the majority of the massive stars in the UCHII phase of evolution. This is an important step in piecing together the evolutionary stages of massive stars in the LMC and what the observables are at each stage. Putting together a self-consistent model of massive star formation in the LMC is possible with a multi-wavelength approach like the one shown here. Such a model would then serve as the basis for star formation studies in galaxies far too distant to resolve individual massive YSOs, revealing aspects about the evolution of the universe never before understood.

Acknowledgements I would like to thank Phil Edwards for allowing use of Director's Time on the Australian Telescope Compact Array. I also acknowledge support from the NASA Rocky Mountain Space Grant and from the Brigham Young University Graduate Fellowship.

Appendix A

Detection of Water Masers Toward Young Stellar Objects in the Large Magellanic Cloud

The following is the paper from Johanson et al. (2014) in its entirety.

The Astrophysical Journal, 781:78 (6pp), 2014 February 1 doi:10.1088/0004-637X/781/2/78

DETECTION OF WATER MASERS TOWARD YOUNG STELLAR OBJECTS IN THE LARGE MAGELLANIC CLOUD

A. K. Johanson[1], V. Migenes[1], and S. L. Breen[2]
[1] Department of Physics and Astronomy, Brigham Young University, N283 ESC, Provo, UT 84602, USA; ajohanson@byu.edu
[2] CSIRO Astronomy and Space Science, Australia Telescope National Facility, P.O. Box 76, Epping NSW 1710, Australia
Received 2013 September 5; accepted 2013 December 9; published 2014 January 10

ABSTRACT

We present results from a search for water maser emission toward N4A, N190, and N206, three regions of massive star formation in the Large Magellanic Cloud (LMC). Four water masers were detected; two toward N4A, and two toward N190. In the latter region, no previously known maser emission has been reported. Future studies of maser proper motion to determine the galactic dynamics of the LMC will benefit from the independent data points the new masers in N190 provide. Two of these masers are associated with previously identified massive young stellar objects (YSOs), which strongly supports the authenticity of the classification. We argue that the other two masers identify previously unknown YSOs. No masers were detected toward N206, but it does host a newly discovered 22 GHz continuum source, also associated with a massive YSO. We suggest that future surveys for water maser emission in the LMC be targeted toward the more luminous, massive YSOs.

Key words: Magellanic Clouds – masers – stars: formation

1. INTRODUCTION

The physical, chemical, and dynamical characteristics of galaxies are generally driven by the intense stellar winds and explosive deaths of high-mass stars within them. Observing these stars in different environments and in various stages of evolution leads to an understanding of the life cycle of these stars and their influence on galactic dynamics. The most poorly understood time of a massive star's life is the early accretionary stage as a young stellar object (YSO; Zinnecker & Yorke 2007). The puzzle of massive star formation is pieced together as these massive stars are found in the early stages of formation as YSOs.

Much of the difficulty in understanding massive star formation lies in finding massive YSOs. This is primarily due to their scarcity, large distances, rapid evolution, and dense, dusty environments. One of the best ways to study star formation is by observing molecular masers around YSOs (e.g., Goddi et al. 2011). The bright, compact radio emission emanating from the masers can be observed at great distances, even through the obscuring dust clouds that hide the environments of the YSOs at visible wavelengths. With the resolution provided by radio interferometry, it is possible to associate masers with individual YSOs, even at the distance of the Large Magellanic Cloud (LMC; Ellingsen et al. 2010). The 22.2 GHz masing transition of water is particularly useful, because it is the strongest transition among known maser species. Water masers are often associated with the outflows of high-mass stars (e.g., see Moscadelli et al. 2000) and thus often indicate the presence of massive YSOs (Beuther et al. 2002), although it is not uncommon for them to be found in the environments of low-mass YSOs (Wilking et al. 1994).

The study of massive star formation in the LMC is particularly useful because many of its physical characteristics differ from those of the Milky Way. For example, the LMC has less mass, a lower star formation rate, no spiral arms, a lower metallicity, and a greater ambient UV flux (Meixner et al. 2006 and references therein), all of which influence star formation on a galactic scale. Previous searches for water masers in the LMC have yielded relatively few detections. The recent paper by Imai et al. (2013) totals the number of detected LMC interstellar water masers at 23 among 14 regions. Green et al. (2008) suggest that the apparent underabundance of water masers in the LMC might be related to the its lower star formation rate (Israel 1980). They also note the difficulty in obtaining a sensitive, full scale survey for water masers in the entire LMC. Searches for these water masers may be more successful if they target known massive YSOs. Gruendl & Chu (2009, hereafter GC09) used infrared data from *Spitzer's* Surveying the Agents of a Galaxy's Evolution (SAGE) program (Meixner et al. 2006) to identify 1385 intermediate- or high-mass YSO candidates based on infrared colors and spectral energy distributions. Of those YSO candidates, they classify 855 as "definite," indicating a high degree of confidence in their nature. Ellingsen et al. (2010) found a high correlation between detected water masers and definite YSO candidates identified by GC09. In fact, 17 of the 23 interstellar masers discovered in the LMC as listed by Imai et al. (2013) are separated by less than 5″ of a GC09 definite YSO. An associated maser with a YSO candidate strongly supports the classification. Therefore, observations toward GC09 YSO candidates may be useful in finding these rare masers and thereby a better understanding of what the presence of water masers tells us about the physical characteristics of YSOs.

We report on observations in search of water masers toward three regions of massive star formation in the LMC. Details on observations and data reduction are found in Section 2. The results of the observations are reported in Section 3, with an analysis of those results given in Section 4. A summary of the results and conclusions is presented in Section 5.

2. OBSERVATIONS

Three regions of massive star formation in the LMC (N4A, N190, and N206; Henize 1956) were observed for the 22.2 GHz water maser line with the Australia Telescope Compact Array (ATCA). Their designations and the pointing positions are listed in Table 1. The ATCA is the radio interferometer in the southern hemisphere with the highest sensitivity and greatest resolution, thus the prime instrument to study the LMC.

Table 1
Targeted Regions

Name[a]	R.A. (J2000) (h m s)	Decl. (J2000) (° ′ ″)	Observing Date
N4A	4 52 09.1	−66 55 14.8	2008 Mar
N190	5 04 25.4	−70 43 49.2	2008 Mar
N206	5 30 23.5	−71 07 04.8	2013 Feb
N206	5 30 48.0	−71 07 55.2	2013 Feb
N206	5 31 00.7	−71 06 54.0	2013 Feb
N206	5 31 22.3	−71 06 54.0	2013 Feb
N206	5 31 22.7	−71 04 11.6	2008 Mar

Notes. The pointing centers for each of the regions of interest.
[a] Designation from Henize (1956).

Archival data were acquired from the Australia Telescope Online Archive. The observation for this data was made on 2008 March 15 (part of program CX139). The ATCA was in its 1.5D configuration, observing at a central frequency of 22.215 GHz with a bandwidth of 16 MHz divided into 512 channels. This gives a spectral channel spacing of 31.25 kHz, yielding a velocity resolution of 0.422 km s^{-1}. The integration time on each source was around 20 minutes over the course of 7 hr.

Additional observations were conducted with the ATCA on 2013 February 9 under program C2773. These observations investigated the N206 region in greater detail. The new data covered four additional pointings in N206 with the 6A array configuration. These observations were taken in an attempt to find water masers associated with 11 definite YSO candidates from GC09, and covered an additional 12.5 arcmin^2 of emission from N206 for a total of ∼15.5 arcmin^2. These observations were taken with two overlapping 2 GHz continuum intermediate frequencies (IFs) giving a total bandwidth of 3 GHz at a central frequency of 22.200 GHz. Since water masers often trace high velocity outflows from YSOs, a wide velocity coverage was necessary. To accomplish this, we utilized the ATCA's capacity to concatenate 16 1 MHz spectral zoom bands in 2 IFs and overlapped them to obtain a total spectral bandwidth of 15.5 MHz, giving a total velocity coverage of ∼210 km s^{-1} around the systemic velocity, sufficient to observe the high-velocity masers. The observations had a high spectral resolution of 0.488 kHz, or a velocity channel spacing of 0.007 km s^{-1}. We then smoothed the data to a velocity resolution of 0.224 km s^{-1} to increase sensitivity. The integration time toward each pointing was 60 minutes over the course of 6 hr.

Both new and archival data were reduced using standard procedures in MIRIAD. PKS B1934−638 was used as the primary amplitude calibrator and had a flux of 0.84 Jy. The flux scale has been determined to an accuracy of ∼10%. One major exception is that for the 2013 data, the primary flux calibrator for the ATCA (PKS B1934−638) was not observable during the course of the observation. Flux calibration was thus done on a secondary calibrator, PKS B0537−441. Based on observations over the past 2 yr, its flux in the *K* band has had an average value of 7.5 Jy, but has varied by ∼25%. We expect a similar error on our amplitude calibration for that data set. PKS B0637−752 was used as the phase calibrator in both experiments, and was observed once every ∼30 minutes for the 2008 data and ∼12 minutes in 2013. The phase calibrator was also used to update the pointing solutions about once an hour. The secondary calibrator flux was bootstrapped from the primary and the amplitude, phase, and bandpass solutions were applied to the program sources.

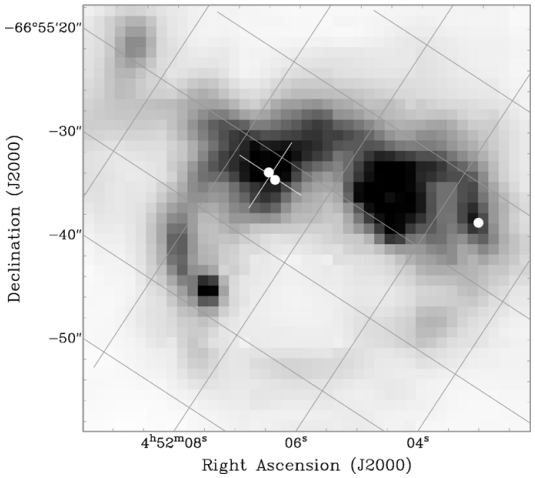

Figure 1. IRAC 8.0 μm image of N4A. The massive YSO identified by GC09 and Contursi et al. (2007) is indicated with a cross. The positions of maser spots detected in this work are shown as white dots. The filamentary structure with the associated maser can be seen as an arc extending to the right of the brightest emission in the region.

Images were made and deconvolved using the CLEAN algorithm using naturally weighted visibilities in order to maximize point-source sensitivity. Image sensitivity for the 2008 observations was ∼7 mJy beam^{-1} rms for N4A and N190, and ∼8.6 mJy beam^{-1} rms for N206. Fortunately, the signal-to-noise ratio for all detected masers in this work is very high. Image sensitivity for the 2013 observations was ∼20 mJy beam^{-1} rms and ∼82 μJy beam^{-1} rms in the maser and continuum images, respectively. Maser positions and peak flux densities were determined by the MIRIAD task IMFIT, which fits two-dimensional Gaussians to the sources. The 2008 1.5D array data had a resolution of about 1.″0 while the 2013 6A array had a resolution of about 0.″5.

3. RESULTS

A total of four masers toward two high-mass star-forming regions were detected. Four maser spots were detected toward N4A and two were detected toward N190. Their positions, properties, and any associated GC09 YSO or Two Micron All Sky Survey (2MASS) point source (Cutri et al. 2003) are reported in Table 2. We judge that a maser is associated with a YSO if it is located within 2″ of the YSO (i.e., the resolution of both the *Spitzer* SAGE survey used by GC09 and 2MASS) after the practice of Ellingsen et al. (2010).

N4A. Three of the four detected maser spots are within 1.″2 of a definite massive YSO candidate identified by GC09 and spectroscopically confirmed by Seale et al. (2009). The other is associated with a region that GC09 and Seale et al. (2009) identify as a "diffuse" source, likely a local enhancement within a filament. The locations of the detected masers relative to the *Spitzer* Infrared Array Camera (IRAC; Fazio et al. 2004) 8.0 μm image are shown in Figure 1. The integrated flux of the central portion of both masers as a function of velocity are displayed in Figure 2.

N190. One of the detected masers is located within 1″ of a GC09 definite massive YSO, also confirmed spectroscopically by Seale et al. (2009). The other maser is farther away, separated

Table 2
Detected H_2O Masers

Source	R.A. (J2000) (h m s)	Decl. (J2000) (° ′ ″)	S_{max}[a] (mJy beam^{-1})	Velocity (km s^{-1})	ΔV (FWHM) (km s^{-1})	Associations	Separation (″)
N4A	04 52 05.24	−66 55 13.9	230 ± 15	262.5	1.0	J045205.39−665513.8[b]	0.9
	04 52 09.05	−66 55 22.5	261 ± 10	259.9	1.0	J045209.22−665521.9[c,d]	1.2
	04 52 09.07	−66 55 22.6	431 ± 30	258.4	1.0	J045209.22−665521.9[c,d]	1.1
	04 52 09.21	−66 55 22.2	275 ± 24	272.5	1.1	J045209.22−665521.9[c,d]	0.3
N190	05 04 24.98	−70 43 42.9	1271 ± 132	231.5	1.3	J050424.82−704343.7[c]	1.1
						J05042500−7043444[e]	1.4
	05 04 25.44	−70 43 41.6	1615 ± 159	231.5	1.3	J05042559−7043434[e]	2.0

Notes. Masers detected in this work. The second and third columns list the positions of the individual maser spots. The fifth and sixth columns give the peak velocity and the FWHM of the best-fit Gaussian to the feature. The last two columns list the relevant associations and the separation of the maser spots from those sources, respectively.
[a] Peak intensity.
[b] Gruendl & Chu (2009) diffuse source.
[c] Gruendl & Chu (2009) massive YSO.
[d] Contursi et al. (2007) Star 2.
[e] Cutri et al. (2003) 2MASS point source.

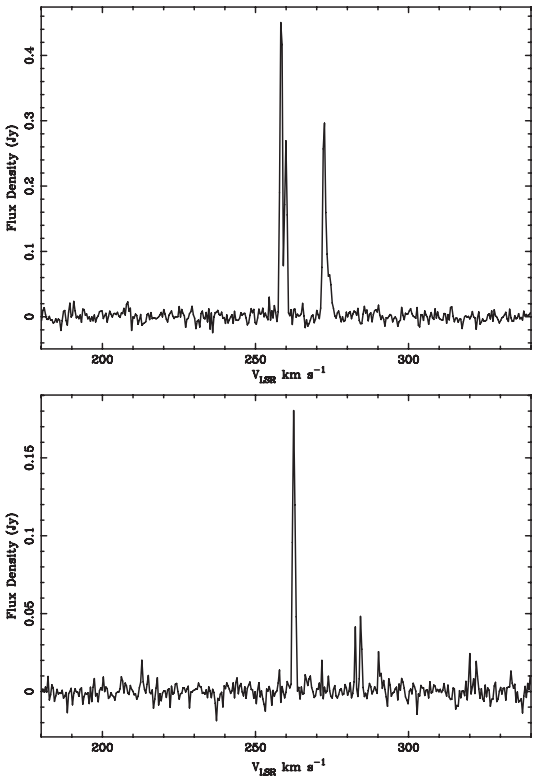

Figure 2. Spectra of the 22.2 GHz water masers toward N4A. Top: the three peaks of maser spots associated with the GC09 massive YSO. Bottom: the maser spot associated with the diffuse filamentary emission. Note that the two small peaks around 283 km s^{-1} are spurious signals due to an incomplete sampling of the *uv* plane.

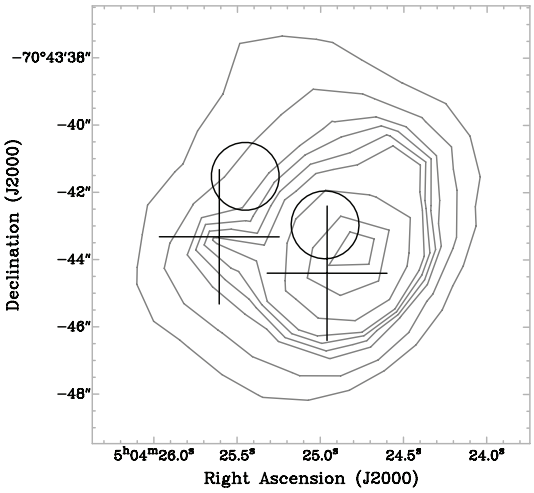

Figure 3. IRAC 4.5 μm contours of N190. Crosses indicate the positions and uncertainties of 2MASS J05042500−7043444 and 2MASS J05042559−7043434. The circles indicate the positions and uncertainties of the newly detected masers. The contours (10%, 15%, 21%, 24%, 27%, 30%, 40%, 60%, and 80% of the peak intensity) have a peak at the GC09 massive YSO, but they do show some emission associated with 2MASS J05042559−7043434 near the other maser.

by about 4″ from the massive YSO, and thus is not considered to be associated with it. The positions of the masers and associated 2MASS point sources are shown against IRAC 4.5 μm continuum contours in Figure 3. The integrated flux of the central portion of both masers as a function of velocity are displayed in Figure 4.

N206. Although no masers were found, a 22 GHz continuum source was detected. Its position and peak flux are reported in Table 3. It is associated with yet another GC09 definite massive YSO confirmed by Seale et al. (2009). Despite the uncertainty in the absolute flux calibration, the 5.5σ signal and association with a known massive YSO indicate that it is a *bona fide* detection. The continuum source position and contours and its relation to the GC09 massive YSO is shown in Figure 5.

4. DISCUSSION

4.1. N4A

N4A is the brightest region in the N4 H II complex. N4A is about 21.″0 in angular size (about 5.0 pc at the 50 kpc distance of

Table 3
Detected Continuum Source

Source	R.A. (J2000) (h m s)	Decl. (J2000) (° ′ ″)	S_{max}[a] (μJy beam^{-1})	rms	S_{int}[b] (μJy)	Association	Separation (″)
N206	05 30 20.16	−71 07 50.3	450	82	636	J053020.33−710748.9[c]	1.6

Notes. Position and flux of the 22 GHz continuum source detected toward N206. The last two columns list the associated massive YSO candidate and its separation from the continuum source, respectively.
[a] Peak intensity.
[b] Total integrated flux.
[c] Gruendl & Chu (2009) massive YSO.

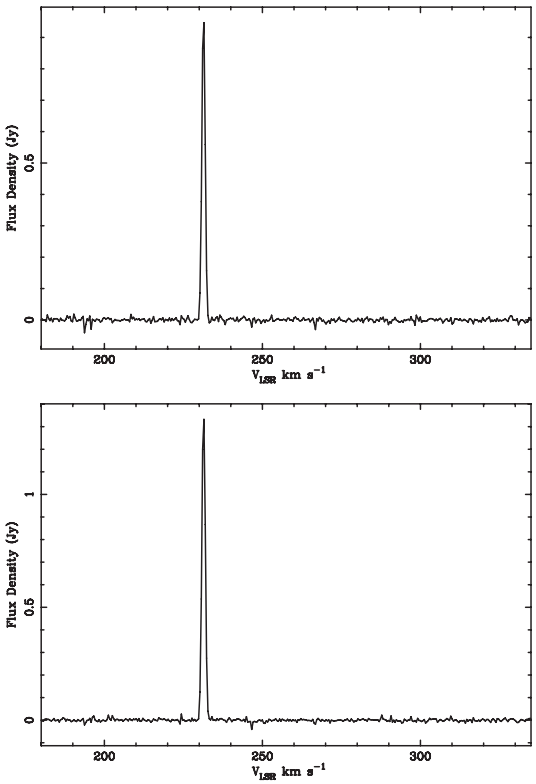

Figure 4. Spectra of the 22.2 GHz water masers toward N190. Top: the maser associated with 2MASS J05042500−7043444. Bottom: the maser associated with 2MASS J05042559−7043434.

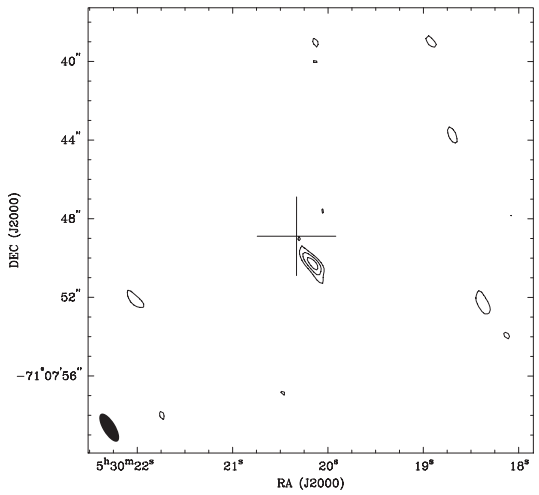

Figure 5. 22.2 GHz contours (at 220, 320, and 420 μJy beam^{-1}) of the continuum source toward N206. The cross indicates the GC09 YSO position and its uncertainty.

the LMC) with two primary ionizing stars (Heydari-Malayeri & Lecavelier des Etangs 1994). Contursi et al. (2007) identified seven stars in the region in their near-infrared images, and suggested that their Star 2, Star 4, and Star 7 are YSOs (keeping with their nomenclature). They correspond to three definite YSOs identified by GC09. We detected three maser spots at different velocities toward Star 2. The feature which peaks at 272.5 km s^{-1} corresponds to the peak CO emission of the "blue" molecular cloud as identified in Heydari-Malayeri & Lecavelier des Etangs (1994). However, it is the "red" component which they believe to be more directly linked with the N4A region. Although it peaks at 278.5 km s^{-1}, it would not be unusual for water masers to be spread by a mere 6 km s^{-1} from the systemic velocity (as is seen in Ellingsen et al. 2010).

Indebetouw et al. (2004) detected radio continuum emission at 4.8 GHz and 8.6 GHz toward Star 2. They suggested from the spectral index that the emission is attributed to thermal emission from an ultracompact H II region caused by an O8 V star. This classification is consistent with a massive central object, but we assert this is still deeply embedded, based on the infrared analysis done by GC09 and Seale et al. (2009), as well as the presence of water masers, which normally indicate an early stage of formation (Ellingsen et al. 2010).

Water maser emission toward N4A had been recently discovered as reported by Imai et al. (2013). They used ATCA archival data from 2003, 5 yr earlier than the data presented here. They likewise detected water masers toward the GC09 massive YSO over a similar velocity range. The spectral characteristics are very different, but high variability is very common for water masers (Felli et al. 2007). Given only the two observations and time between them, it is impossible to know all the details of their variability. We can only assume that the maser emission here has been somewhat persistent at least over a 5 yr period (i.e., 2003–2008).

The maser spot peaking at 262.5 km s^{-1} is not associated with a YSO candidate or any radio continuum emission detected by Indebetouw et al. (2004), nor was it detected in the archival data by Imai et al. (2013; which may be simply due to variability).

There is an infrared source detected in the *Spitzer* 3–8 μm IRAC data, but not at longer wavelengths, and there is also no associated 2MASS near-infrared point source. GC09 classified it as a diffuse source (J045205.39−665513.8) on the basis of it having no near- or far-infrared counterpart, and the fact that it is embedded in the aforementioned dust filament. The filamentary structure was identified by Heydari-Malayeri & Lecavelier des Etangs (1994). Even the spectral analysis by Seale et al. (2009) initially classified it as a highly embedded YSO, but they argued in favor of the GC09 interpretation, noting that such diffuse objects are "spectroscopically indistinguishable from YSOs" in that limited spectral range.

Given the corresponding infrared evidence, our detection of a water maser is strong evidence that this source is indeed a YSO. It is interesting to note that GC09 state that their diffuse sources may harbor low- or intermediate-mass YSOs. It is not uncommon for low-mass YSOs to exhibit water maser emission (Wilking et al. 1994, for example), but it would be the first detection of an extragalactic maser associated with a low-mass YSO (Imai et al. 2013). However, GC09 and Seale et al. (2009) both use the criterion that to first order, YSOs with an IRAC 8.0 μm magnitude less than eight ([8.0] $<$ 8.0 mag) indicates they are high-mass. For J045205.39−665513.8, [8.0] $=$ 7.74. In addition, Ellingsen et al. (2010) found that water maser emission in the LMC occurs preferentially toward the more luminous and redder GC09 definite YSOs. They identified criteria in color–magnitude space which identify regions where maser sources are most likely to be found, and the J045205.39−665513.8 colors satisfy these criteria. Although more study will be needed to determine its mass, we are certain it is a YSO.

4.2. N190

The emission nebula N190 is a poorly studied, inconspicuous H II region near the NGC 1833 star cluster. Of the two masers detected here, one of them is associated with a GC09 massive YSO, but the other is about 4″ away. We investigated the 2MASS point-source catalog and found two sources, one which is the massive YSO (J05042500−7043444), but also another source (J05042559−7043434) that is separated from the far maser by 2″. Since the resolution of the 2MASS survey is 2″, we claim that this far maser is associated with it. 2MASS J05042559−7043434 has a very faint counterpart in the IRAC 4.5 μm data (Figure 3), but not in the other IRAC bands. This is reminiscent of extended green objects (EGOs) seen in the Milky Way, extended regions of emission often indicating shocked gas from massive YSO outflows (Cyganowski et al. 2013). Finding water masers toward these EGOs has been met with great success, where Cyganowski et al. (2013) detected water masers toward 68% of these structures. Naturally at the distance of the LMC, we do not have the resolution to determine if the source is a genuine EGO, but the associated 4.5 μm emission enhancement and water maser lead us to believe that 2MASS J05042559−7043434 is a previously undiscovered massive YSO.

The masers in N190 are new detections. They will be particularly beneficial to studies that propose to determine some of the dynamics of the LMC, such as the project discussed by Imai et al. (2013). With very long baseline interferometry and a sufficient number of masers, a statistical analysis of the maser proper motions can be used to determine the motion and galactic rotation of the LMC. With only small number of masers, each new star-forming region with masers will significantly improve such studies, each providing an additional three observables to fit to a dynamical model. More significantly, N190 is spatially separated from other known maser regions, useful in removing any degeneracy in the model fitting by sampling that area of the LMC. The nearest masers are separated by over 1°.5, thus it is an essential probe of the galactic dynamics in that region. Including the new maser in N4A, these discoveries bring the total number of interstellar water masers in the LMC from 23 in 14 regions (Imai et al. 2013) to 26 in 15 regions.

4.3. N206

N206 is a high-mass star-forming region, where most of the star formation occurs along a molecular ridge at the edge of a superbubble formed by supernova shocks and massive stellar winds (Dunne et al. 2001; Kavanagh et al. 2012). Besides GC09, other groups have identified massive YSOs in N206, but with different results (i.e., GC09 identified 23, while Romita et al. 2010 and Carlson et al. 2012 identified 116 and 73, respectively). A search toward the five pointings in this region for water masers yielded a null detection down to around 20 mJy rms, thus we were unable to provide supporting evidence for these YSO candidates.

We do report detection of continuum emission at 22 GHz (Table 3) toward a GC09 massive YSO. Remarkably, neither Romita et al. (2010) nor Carlson et al. (2012) identified this source as a YSO candidate. Indebetouw et al. (2004) detected continuum emission at 4.8 GHz and at 8.6 GHz at this same location, but they determined a spectral index for a source slightly north of the massive YSO. Follow-up observations will be needed to determine a spectral index and thus the nature of the emission (i.e., whether it is thermal from a compact H II region).

5. SUMMARY

A search for 22.2 GHz water masers from archival data toward three massive star-forming regions in the LMC resulted in the detection of four masers toward two regions. Three of these are new detections, bringing to date the total number of water masers around young stars in the LMC to 26 in 15 regions. New observations of N206 yielded no maser detections, but did reveal the presence of 22 GHz continuum emission, coincident with previously detected emission at lower frequencies (Indebetouw et al. 2004).

Two of the masers and continuum source are associated with massive YSOs identified by GC09 and confirmed by Seale et al. (2009), providing strong supporting evidence for their classification. One of the other masers was discovered toward a GC09 diffuse source in N4A, and one toward a 2MASS point source in N190. We assert that these masers are signaling the presence of YSOs. All the GC09 sources have 8.0 μm magnitudes less than 8.0, and have redder IRAC colors when compared to the YSO candidate sample as a whole. This supports the conclusions of Ellingsen et al. (2010), namely that massive YSOs with associated water maser emission are more luminous and have redder colors, indicating highly embedded objects. The other maser in N190 is not very bright in the IRAC bands, and therefore was not included in the GC09 survey. All in all, the methods used by GC09 appear to be successful in identifying massive YSOs. We recommend future surveys for water masers should target luminous, definite GC09 YSO candidates with infrared excess.

We thank Phil Edwards for allowing us Director's Time on the Australian Telescope Compact Array. The Australia Telescope is funded by the Commonwealth of Australia for operation as a National Facility managed by CSIRO. We also acknowledge support from the NASA Rocky Mountain Space Grant and from the Brigham Young University Graduate Fellowship.

Facilities: Spitzer, ATCA

REFERENCES

Beuther, H., Walsh, A., Schilke, P., et al. 2002, A&A, 390, 289
Carlson, L. R., Sewiło, M., Meixner, M., Romita, K. A., & Lawton, B. 2012, A&A, 542, 66
Contursi, A., Rubio, M., Sauvage, M., et al. 2007, A&A, 469, 539
Cutri, R. M., Skrutskie, M. F., van Dyk, S., et al. 2003, yCat, 2246, 0
Cyganowski, C. J., Koda, J., Rosolowsky, E., et al. 2013, ApJ, 764, 61
Dunne, B. C., Points, S. D., & Chu, Y. 2001, ApJS, 136, 119
Ellingsen, S. P., Breen, S. L., Caswell, J. L., Quinn, L. J., & Fuller, G. A. 2010, MNRAS, 404, 779
Fazio, G. G., Hora, J. L., Allen, L. E., et al. 2004, ApJS, 154, 10
Felli, M., Brand, J., Cesaroni, R., et al. 2007, A&A, 476, 373
Goddi, C., Moscadelli, L., & Sanna, A. 2011, A&A, 535, L8
Green, J. A., Caswell, J. L., Fuller, G. A., et al. 2008, MNRAS, 385, 948
Gruendl, R. A., & Chu, Y. 2009, ApJS, 184, 172
Henize, K. G. 1956, ApJS, 2, 315
Heydari-Malayeri, M., & Lecavelier des Etangs, A. 1994, A&A, 291, 960
Imai, H., Katayama, Y., Ellingsen, S. P., & Hagiwara, Y. 2013, MNRAS, 432, L16
Indebetouw, R., Johnson, K. E., & Conti, P. 2004, AJ, 128, 2206
Israel, F. P. 1980, A&A, 90, 246
Kavanagh, P. J., Sasaki, M., & Points, S. D. 2012, A&A, 547, 19
Meixner, M., Gordon, K. D., Indebetouw, R., et al. 2006, AJ, 132, 2268
Moscadelli, L., Cesaroni, R., & Rioja, M. J. 2000, A&A, 360, 663
Romita, K. A., Carlson, L. R., Meixner, M., et al. 2010, ApJ, 721, 357
Seale, J. P., Looney, L. W., Chu, Y., et al. 2009, ApJ, 699, 150
Wilking, B. A., Claussen, M. J., Benson, P. J., et al. 1994, ApJ, 431, 119
Zinnecker, H., & Yorke, H. W. 2007, ARA&A, 45, 481

Bibliography

Alves, David R. 2004, ApJ, 601, L151

Bartkiewicz, A., Szymczak, M., van Langevelde, H. J., Richards, A. M. S., & Pihlström, Y. M. 2009, A&A, 502, 155

Bock, D. C. J., Large, M. I., & Sadler, E. M. 1999, AJ, 117, 1578

Bonanos, A. Z., Massa, D. L., Sewiło, M., et al. 2009, AJ, 138, 1003

Breen, S., Ellingsen, S., Contreras, Y., et al. 2013, MNRAS, 435, 524

Churchwell, E. 2002, ARAA, 40, 27

Contursi, A., Rubio, M., Sauvage, M., et al. 2007, A&A, 469, 539

Crowther, P. A. 2005, IAUS, 227, 389

Cutri, R. M., Skrutskie, M. F., van Dyk, S., et al. 2003, VizieR Online Data Catalog, 2246

Cyganowski, C. J., Koda, J., Rosolowsky, E., et al. 2013, ApJ, 764, 61

Dickel, John R., McIntyre, Vincent J., Gruendl, Robert A., & Milne, Douglas K. 2005, AJ, 129, 790

Dunne, B. C., Points, S. D., & Chu, Y. 2001 ApJS, 136, 119

Ellingsen, S. P., Breen, S. L., Caswell, J. L., Quinn, L. J., & Fuller, G. A. 2010, MNRAS, 404, 779

Elmegreen, Bruce G., & Lada, Charles J. 1977, ApJ, 214, 725

Felli, M., Brand, J., Cesaroni, R., et al. 2007, A&A, 476, 373

Flesch, E., & Hardcastle, M. J. 2004, A&A, 427, 387

Goddi, C., Moscadelli, L., & Sanna, A. 2011, A&A, 535, L8

Gorjian, V., Werner, M. W., Mould, J. R., et al. 2004, ApJS, 154, 275

Green, J. A., Caswell, J. L., Fuller, G. A., et al. 2008, MNRAS, 385, 948

Gruendl, R. A., & Chu, Y. 2009, ApJS, 184, 172

Harris, Jason, & Zaritsky, Dennis, 2009, AJ, 138, 1243

Henize, K. G. 1956, ApJS, 2, 315

Heydari-Malayeri, M., & Lacavelier des Etangs, A. 1994, A&A, 291, 960

Imai, H., Katayama, Y., Ellingsen, S. P., & Hagiwara, Y. 2013, MNRASL, 432, L16

Indebetouw, R., Johnson, K. E., & Conti, P. 2004, AJ, 128, 2206

Johanson, A. K., Migenes, V., & Breen, S. L. 2014, ApJ, 781, 78

Kavanagh, P. J., Sasaki, M., & Points, S. D. 2012, A&A, 547, 19

Kozłowski, S., & Kochanek, C. S. 2009, ApJ, 701, 508K

Kraus, S., Hofmann, K., Menten, K., et al. 2010, *Nature*, 466, 339

Martín-Hernández, N. L., van der Hulst, J. M., & Tielens, A. G. G. M. 2003, A&A, 407, 957

Menten, Karl M. 1991, ApJ, 380, 75

McKee, Christopher F., & Ostriker, Eve C. 2007, ARA&A, 45, 565

Meixner, M., Gordon, K. D., Indebetouw, R., et al. 2006, AJ, 132, 2268

Mezger, P. G., & Henderson, A. P. 1967, ApJ, 147, 471

Reid, M. J., Menten, K. M., Zheng, X. W., et al. 2009, ApJ, 700, 137

Robitaille, Thomas P., Whitney, Barbara A., Indebetouw, Remy, Wood, Kenneth, & Denzmore, Pia 2006, ApJS, 167, 256

Robitaille, Thomas P., Whitney, Barbara A., Indebetouw, Remy, & Wood, Kenneth 2007, ApJS, 169, 328

Robitaille, Thomas P., & Whitney, Barbara A. 2010, ApJ, 710, 11

Rodríguez, L. F., Carrasco-González, C., Montes, G., & Tapia, M. 2014, AJ, 148, 20

Salpeter, Edwin E. 1955, ApJ, 121, 161

Sanders, D. B. 1999, IAUS, 194, 25

Seale, J. P., Looney, L. W., Chu, Y., et al. 2009, ApJ, 699, 150

Selier, R., & Heydari-Malayeri, M. 2012, A&A, 545, 29

Smith, R. C., & MCELS Team 1998, PASA, 15, 163

Stern, D., Eisenhardt, P., Gorjian, V., et al. 2005, ApJ, 631, 163

Weaver, Harold, Williams, David R. W., Dieter, N. H., & Lum, W. T. 1965, *Nature*, 208, 29

Wilking, B. A., Claussen, M. J., Benson, P., J., et al. 1994, ApJ, 431, 119

Wood, Douglas O. S., & Churchwell, Ed 1989a, ApJS, 69, 831

Wood, Douglas O. S., & Churchwell, Ed 1989b, ApJ, 340, 265

Zaritsky, D., Harris, J., Thompson, I. B., & Grebel, E. K. 2004, A&A, 128, 1606

Zinnecker, H., & Yorke, H. W. 2007, ARA&A, 45, 481